LIGHT SCATTERING IN THE OCEAN AND IN BIOLOGICAL TISSUES

A Dissertation

by

DAYOU CHEN

Submitted to the Office of Graduate and Professional Studies of
Texas A&M University
in partial fulfillment of the requirements for the degree of

DOCTOR OF PHILOSOPHY

Chair of Committee,	George W. Kattawar
Committee Members,	Roland E. Allen
	Edward S. Fry
	Ping Yang
Head of Department,	George R. Welch

December 2016

Major Subject: Physics

ABSTRACT

In the first part of this dissertation, we simulate the underwater polarized light field. A three-dimensional backward Monte Carlo code is developed to simulate light scattering for an atmosphere-ocean system. In this model, we send photons from the detector and propagate them toward the source, which allows us to calculate the effective Mueller Matrix of the medium. The 3D vector radiation field can be calculated with dynamic interface, complex boundary conditions, as well as the complex ocean objects included in the system. The polarizer imaging is first modeled when polarizers are stuck on the surface of a piece of mirror and put in the open ocean to study the light polarizations in the ocean water. The effects of observation distance and viewing angle on the radiance, the degree of polarization, as well as the angle of polarization are studied systematically. Then we use a simple tank model, where several spheres of different sizes and different scattering properties were placed, to simulate what a marine organism can see under the water. Images based on four different Stokes components are obtained for a variety of underwater circumstances.

In the second part, we study the effect of both coherent and incoherent beams on both forward and multiple scattering of particulate media in biological tissues. The phase shift of a single particle in the forward direction is calculated using the anomalous diffraction method; the influence of particle size distributions, particle shapes, and particle orientations on the forward coherent peaks is studied for an ensemble of particles. In particular, we demonstrate the forward coherent scattering, as well as multiple scattering properties in detail for the chromatophore cell in cephalopods and the human blood system. Additionally, Mueller matrix components with partially coherent or even non-coherent incident beams are investigated in order to study the effect of coherence length on the forward

coherent scattering and multiple scattering.

DEDICATION

To my family, teachers and friends.

ACKNOWLEDGMENTS

First, I would like to express sincere gratitude to my advisors, Dr. George W. Kattawar. His continuous support, his patience and his insight into immense knowledge help me a lot, not only in my research, but also in my life. His enthusiasm to science deeply inspires me.

Then, I would like to thank my committee members, Dr. Ping Yang, Dr. Edward S. Fry and Dr. Roland E. Allen. Thank for their suggestions and support throughout the course of my research.

At last, I would like to say thank you to Dr. Bingqiang Sun, Xin Huang, Jianping Liu and Meng Gao. Thanks for their help and working with them is joyful. Thanks also go to my colleagues, my friends, and the department faculties and staffs.

TABLE OF CONTENTS

LIST OF FIGURES

x

xi

1. INTRODUCTION[*]

1.1 Simulating the underwater polarized light field

Underwater imaging is challenging due to the significant attenuation of light caused by absorption and scattering of hydrosols and marine organism in the ocean [1, 2, 3, 4, 5]. Active illumination is usually required to get improved visibility [1, 2, 3, 4]. Since the unpolarized sunlight will be polarized after scattering [6], using polarization properties of light is one of the options to improve the imaging quality in the ocean [7, 2, 4, 5]. In addition, many marine animals are sensitive to polarized light and are able to use the light polarization information. For example, anchovies can use polarization to detect zooplankton and to navigate [8]; squids have a polarization visual system to aid them to discover some transparent plankton [9, 10] and to communicate with each other [11]; and stomatopods are even capable of sensing circularly polarized light [12]. A good model is needed to simulate underwater polarized light field to study impact of polarization on underwater imaging as well as on marine animals.

The radiative transfer theory [13, 14] has been widely used to calculate the polarized light field in the atmosphere and ocean. Due to polarization, the vector radiative transfer equations need to be solved. Many of the calculations are limited to plane-parallel systems [15, 16, 17, 18], where the scattering medium is assumed to be in one dimension along the vertical direction and homogeneous in the other two dimensions. The three-dimensional (3D) solutions to the vector radiative transfer equations [19, 20, 21, 22] can provide more predictions to real situations. Impulse response solutions for the 3D atmosphere-ocean system with a dynamic surface has obtained through the hybrid matrix operator-Monte

---

[*]Figure 1.1 is reprinted with permission from "Ultrastructure of cephalopod chromatophore organs" by Cloney, Richard A., and Ernst Florey, 1968, Cell and Tissue Research 89.2 , 250-280, Copyright 1968 by Springer.

Carlo method [23, 24, 25]. However, no marine organisms have even been placed in the medium to consider their interactions with the surrounding light field in these methods. An object placed in the scattering medium will destroy the symmetry and make the calculation much more complex. We seek a Monte Carlo model to calculate the 3D vector radiation field for an atmosphere-ocean system, which includes the dynamic interface, complex boundary conditions as well as complex ocean objects. The code will be used to simulate underwater imaging for the real underwater environment.

1.2 Effect of both coherent and incoherent beams on both forward and multiple scattering for an ensemble of particles

Granular materials with organic particles densely packed together are abundant in many biological organisms. Chromatophore cells [26, 27] are one type of coloration cells under the skin of cephalopods, which play an important role for the astonishing camouflage ability of cephalopods. The basic chromatophore cell consists of many pigment granules (chromatosomes) surrounded by a filamentous compartment (elastic sacculus) with radial muscle fibers attached around the circumference, as shown in Figure 1.1. These pigment granules are highly spherical with a diameter about 300nm and the muscle fibers can control the cell to expand or contract, thereby changing the granules density and the color of the cell. Another example is the human blood system. There are several kinds of cells immersed in the blood plasma [28], among which erythrocytes are the most abundant ones. These erythrocytes are also nearly spherical with a diameter of several microns and occupy about 40%-45% of blood by volume. The interactions between the filling particles make it very complex to calculate the scattering properties of such systems. One can always observe a big forward-scattering peak caused by constructive interference [29], as well as many distinct multiple scattering effects. Since the filling particles are spherical, we can model the chromatophore cell or the blood system in the form of an imaginary
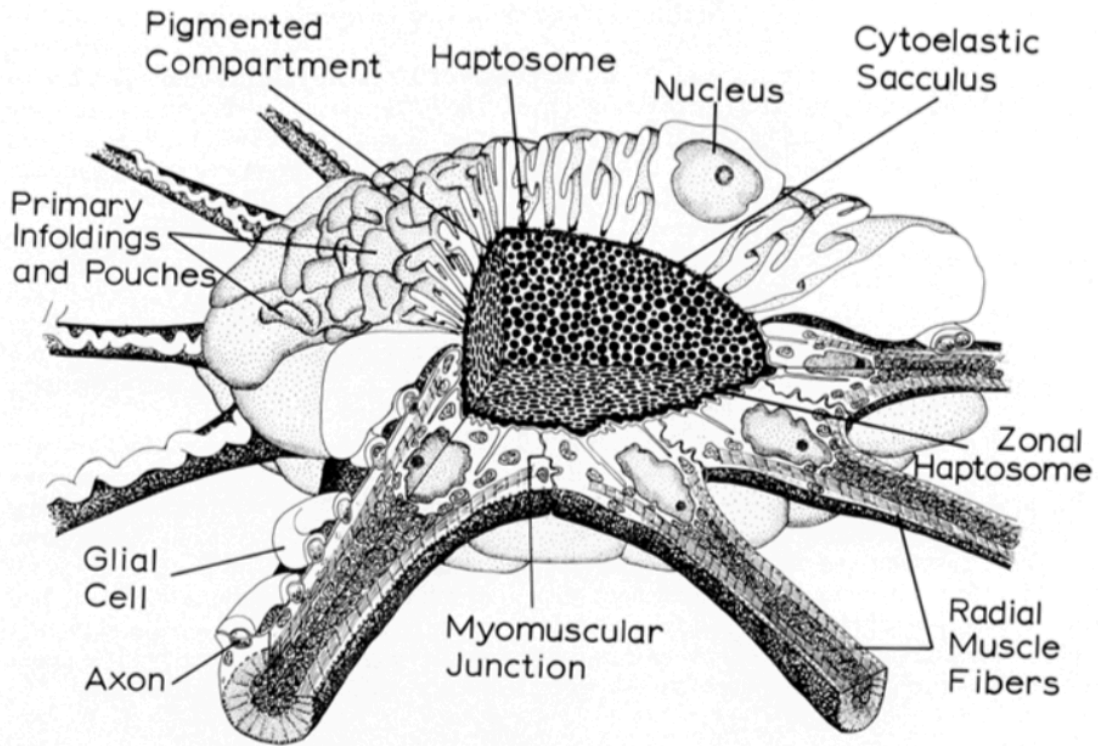
Figure 1.1: Diagrammatic illustration of a squid chromatophore cell. It consists of many pigment granules (chromatosomes) surrounded by a filamentous compartment (elastic sacculus) with radial muscle fibers attached around the circumference.

spherical volume enclosing many small spheres, as shown in Figure 1.2. Note all organic particles are immersed in the ambient media of tissue, which has a refractive index close to that of water (n=1.33), thus we consider all incident wavelengths and refractive indices are relative to the ambient medium. The specific refractive indices of these filling particles vary a great deal in different circumstances, while for simplicity we assume they have the same values relative to the surrounding medium: 1.244+i0.013 for the chromatosomes [30] and 1.0226+i0.001 for erythrocytes [31]. Exact scattering results are compared with results with approximations, in an effort to search for simple simulation models for the complex scattering media.

3
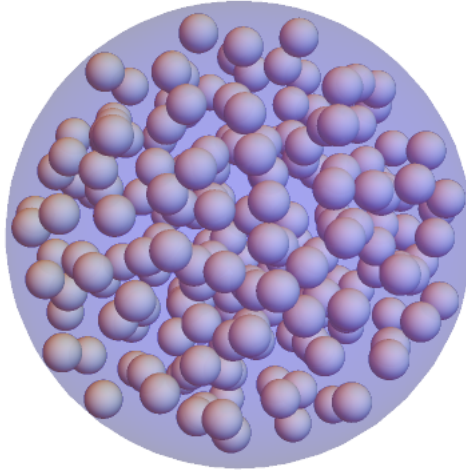
Figure 1.2: Modeled chromatophore cell or blood system by an imaginary spherical volume enclosing many small spheres.

The scattering properties of single particles has been thoroughly studied, and many numerical methods have been well developed, such as the Lorenz-Mie theory [32], the discrete dipole approximation (DDA) method [33, 34], the finite difference time domain (FDTD) method [35, 36], and the invariant imbedding T-matrix (IITM) method [37, 38]. For a particulate medium containing an ensemble of particles, there are two distinct approaches to deal with the multiple scattering problem: radiative transfer theory (or transport theory) and analytical theory (or multiple scattering theory) [39]. Radiative transfer theory [13, 14] deals directly with the transport of energy through the medium, and thus assumes the scattering events are independent and therefore no phase information is used. This implies that an ensemble of N particles will produce a scattered radiance of N times

4

that for a single particle in the ensemble assuming of course the particles are identical and only single scattering is important. This method has been well established to solve the scattering problems in the atmosphere, the ocean, and in biological media. In contrast, analytical theory [39], such as Twersky's theory and the diagrammatic method, is mathematically rigorous since it starts with basic differential equations governing field quantities and includes all the multiple scattering, diffraction, and interference effects. However, until now no solution exists to get the explicit exact formulations to include all these effects, and approximations are needed to get useful solutions for different ranges of parameters. Currently, there does not exist a versatile and numerically accurate method for the scattering solutions of ensembles of particles with arbitrary shape and size. The DDA and the FDTD methods are feasible ways to get the scattering results for small numbers of particles with relatively small size parameters; the multiple sphere T-matrix (MSTM) method [40] can provide a numerically exact solution for the scattering of a large number of spherical particles. These are the analytic methods mainly used.

The incident light is always assumed to be fully coherent in many light scattering theories [32, 33, 34, 35, 36, 40]. But in reality, light always has some degree of incoherence due to light source fluctuations and interactions with the surrounding medium. The natural sunlight, which is the direct light source for many oceanic and atmospheric measurements, has a spatial coherence length of about 60um and a temporal coherence length of the order of 1um [41]. A laser beam, which is often used as a light source in the laboratory and in remote sensing, is fully spatially coherent throughout the cross-sectional width of the beam and partially temporally coherent with a coherence length of the order of 100km, and thus can be treated as coherent source WolfEmil. But it will become partially coherent after propagating through atmospheric turbulence when it is used in remote sensing [42]. Spreading of partially coherent beams in random media has been studied [39, 42, 43], however, the partial coherence effect on the scattering of an ensemble of particles has

5

received little attention. When people make measurements of light scattering, the finite coherence length of the source has constantly been neglected. We will account for the finite coherence effect for the scattering of an ensemble of particles in the last part of this dissertation.

2. SCATTERING GEOMETRY:STOKES VECTOR AND MUELLER MATRIX

In this chapter, we will introduce the geometry and mathematical formalism that are usually used to describe the scattering problems.

2.1 Radiance and irradiance

There are several fundamental quantities which can be used to characterize the energy distribution of the radiation field. The radiance, or the specific intensity, I_ν, is the most important one. The radiance [13] at position $\vec{r}$ in direction $\hat{\Omega}$ is defined as the energy flowing across an element area dA within the solid angle $d\Omega$, in the frequency interval $(\nu, \nu + d\nu)$, during a time interval dt:

$$dE_\nu = I_\nu(\vec{r}, \hat{\Omega}, \nu, t) \, cos\theta \, d\nu dA d\Omega dt \tag{2.1}$$

where θ is the angle between the surface normal direction and the radiance direction $\hat{\Omega}$.

Another important quantity is the irradiance [13], or the net flux, F_ν, which is defined as the flux density flowing across an unit area. Actually it is just the net flow in all the directions and can be obtained by an integration over all solid angles:

$$F_\nu = \int_\Omega I_\nu(\hat{\Omega}) \, cos\theta \, d\Omega \tag{2.2}$$

2.2 Description of the light: Stokes vector

The electric field of a light beam can be very complex. But it can always be represented by a superposition of plane waves in terms of a Frourier transformation [44]. To simplify our problem, we can assume the the incident wave to be a plane wave. This is because Maxwell equations are linear. We can first solve the plane wave incidence and then use

7

superposition to get the solution to the scattering problem for any kind of incident beams.

The electric field is transverse and it can be decomposed into two perpendicular components due to its polarization nature, as shown in Figure 2.1. A plane of reference is needed to conveniently describe the scattering of a beam of light. Typically, we choose the plane of reference in a way such that the direction of propagation $\hat{k}$ is in the plane of reference. Then we can define two unit vectors: $\hat{e}_\parallel$ and $\hat{e}_\perp$, which are parallel and perpendicular to the reference plane respectively, but both perpendicular to $\hat{k}$. The relationship between the three unit vectors can be expressed as:

$$\hat{e}_\perp \times \hat{e}_\parallel = \hat{k} \tag{2.3}$$

Then the electric field in terms of the two perpendicular components $E_\parallel$ and $E_\perp$ in vector form is:

$$\mathbf{E} = E_\parallel \hat{e}_\parallel + E_\perp \hat{e}_\perp \tag{2.4}$$

Note we only require the plane of reference to contain $\hat{k}$ and thus we have one degree of freedom to choose any pair of $\hat{e}_\parallel$ and $\hat{e}_\perp$ which satisfy Eq. (2.3), i.e. one degree of freedom to choose any plane of reference. Two kinds of reference planes are mainly used in many light scattering theories: the scattering plane (indicated in blue in Figure 2.1), which contains the incident and scattered directions; and the meridian plane (indicated in pink in Figure 2.1), which contains the z-axis of the laboratory frame of reference and the incident or scattered directions.

The transformation of electric field between different reference planes can be realized by a rotation from the original reference plane to the final reference plane around the propagation direction $\hat{k}$. Such a rotation of angle θ in the counterclockwise direction
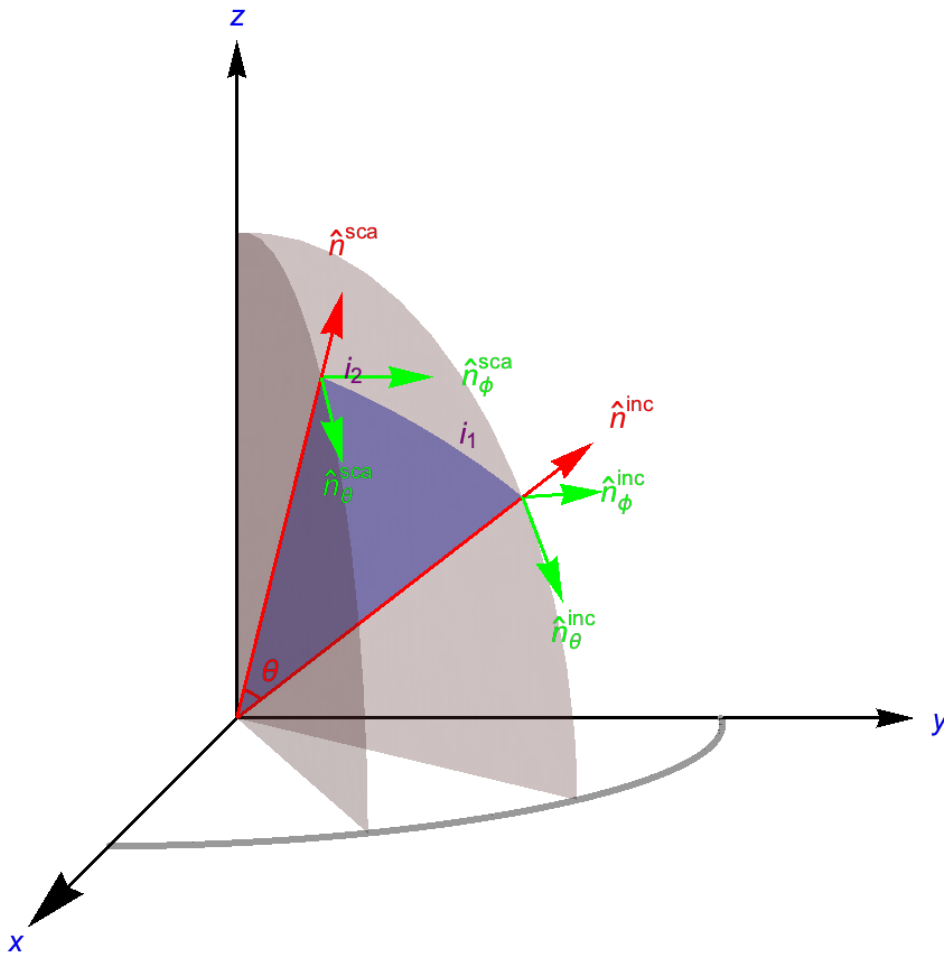
Figure 2.1: Reference planes and the decomposition of the incident and scattered electric fields within the meridional planes. The scattering plane (indicated in blue) contains the incident and scattered directions; and the meridian plane (indicated in pink) contains the z-axis of the laboratory frame of reference and the incident or scattered directions. In the meridional planes, $\hat{e}_\perp = -\hat{n}_\phi$, $\hat{e}_\parallel = \hat{n}_\theta$, $\hat{k} = \hat{n}$.

around $\hat{k}$ will rotate the unit vectors $\hat{e}_\parallel$ and $\hat{e}_\perp$ according to

$$\begin{pmatrix} \hat{e}'_\parallel \\ \hat{e}'_\perp \end{pmatrix} = \begin{pmatrix} cos\theta & sin\theta \\ -sin\theta & cos\theta \end{pmatrix} \begin{pmatrix} \hat{e}_\parallel \\ \hat{e}_\perp \end{pmatrix} \tag{2.5}$$

Thus the electric field will transform according to

$$\begin{pmatrix} E'_\parallel \\ E'_\perp \end{pmatrix} = \begin{pmatrix} cos\theta & -sin\theta \\ sin\theta & cos\theta \end{pmatrix} \begin{pmatrix} E_\parallel \\ E_\perp \end{pmatrix} \tag{2.6}$$

The electric fields are usually difficult to measure directly, instead it's much easier to make measurements in terms of the energy. Thus it's more practical to use the Stokes vector $\mathbf{I} = (I, Q, U, V)^T$ [44] which is based on energy flux and defined as:

$$\begin{aligned} I &= < E_\parallel E_\parallel^* + E_\perp E_\perp^* > \\ Q &= < E_\parallel E_\parallel^* - E_\perp E_\perp^* > \\ U &= < E_\parallel E_\perp^* + E_\perp E_\parallel^* > \\ V &= i < E_\parallel E_\perp^* - E_\perp E_\parallel^* > \end{aligned} \tag{2.7}$$

where $<>$ indicates time average over an interval long compared with the period. We can directly measure the four Stokes components [44]. The Stokes vector has dimensions of irradiance and all its four components are real. It can also be shown that:

$$I \; > \; 0, \tag{2.8}$$

$$I^2 \; \geq \; Q^2 + U^2 + V^2. \tag{2.9}$$

Equality holds only when the light is polarized. When the light is unpolarized, the Stokes vector reduces to $(I, 0, 0, 0)^T$. For more general state of polarization, we can define the

degree of polarization (DOP), the degree of linear polarization (DOLP) and degree of circular polarization (DOCP):

$$DOP = \sqrt{Q^2 + U^2 + V^2}/I, \tag{2.10}$$

$$DOLP = \sqrt{Q^2 + U^2}/I, \tag{2.11}$$

$$DOCP = V/I. \tag{2.12}$$

All the three quantities are bounded in [0,1] and they can be used to characterize the polarization properties of the light field.

Then the transformation of Stokes vectors from the original reference plane to the new reference plane by a rotation of angle θ in the counterclockwise direction around $\hat{k}$ can be obtained by substituting Eq. (2.6) into Eq. (2.7):

$$\mathbf{I}' = \mathbf{L}(\theta)\mathbf{I} \tag{2.13}$$

and

$$\mathbf{L}(\theta) = \begin{pmatrix} 1 & 0 & 0 & 0 \\ 0 & cos(2\theta) & sin(2\theta) & 0 \\ 0 & -sin(2\theta) & cos(2\theta) & 0 \\ 0 & 0 & 0 & 1 \end{pmatrix} \tag{2.14}$$

We can easily find three invariables under the transformation: $I, Q^2 + U^2, and\ V$. In other words, these three quantities are independent on the reference plane.

2.3 Description of the scatterer: Amplitude matrix and Mueller matrix

For a scatter with finite size, the scattered electric field in the far-field region is a transverse spherical wave [44]:

$$\mathbf{E}^{sca} = \frac{e^{ikr}}{-ikr}\mathbf{A}, \quad kr \gg 1 \tag{2.15}$$

where $\mathbf{A}$ is the amplitude of scattered electric field, r is the radial coordinate, $k = 2\pi/\lambda$ is the wavenumber and λ is the incident wavelength. Again due to the linearity of Maxwell equations, the relation between the incident and scattered electromagnetic fields in Figure 2.1 is linear. Mathematically, we can write it as[44, 45]:

$$\begin{pmatrix} E_\parallel^{sca} \\ E_\perp^{sca} \end{pmatrix} = \frac{e^{ik(r-z)}}{-ikr} \begin{pmatrix} S_2 & S_3 \\ S_4 & S_1 \end{pmatrix} \begin{pmatrix} E_\parallel^{inc} \\ E_\perp^{inc} \end{pmatrix} \tag{2.16}$$

Here matrix $\mathbf{S}$ is defined as the amplitude matrix, with the incident direction along the z-axis in the laboratory frame. The amplitude matrix contains all the scattering information of the scatterer and is independent of both the incident fields and the scattered fields. There are eight independent constants contained by the four complex elements. However, since only relative phase matters, we actually have seven independent constants here.

By substituting Eq. (2.16) into Eq. (2.7), we can get the 4×4 so-called Mueller matrix $\mathbf{P}$, which relates the incident Stokes vector $\mathbf{I}_i$ and the scattered Stokes vector $\mathbf{I}_s$:

$$\mathbf{I}_s = \frac{1}{k^2 r^2}\mathbf{P}\,\mathbf{I}_i \tag{2.17}$$

The Mueller matrix $\mathbf{P}$ can be derived directly from the scattering amplitude matrix $\mathbf{S}$ [46]:

$$\mathbf{P} = \mathbf{A}(\mathbf{S} \otimes \mathbf{S}^*)\mathbf{A}^{-1} \tag{2.18}$$

Here $\otimes$ denotes the outer product of matrices and the matrix $\mathbf{A}$ is the given by:

$$\mathbf{A} = \begin{pmatrix} 1 & 0 & 0 & 1 \\ 1 & 0 & 0 & -1 \\ 0 & 1 & 1 & 0 \\ 0 & i & -i & 0 \end{pmatrix}, \quad \mathbf{A}^{-1} = \frac{1}{2}\mathbf{A}^* \tag{2.19}$$

Here $\mathbf{A}^*$ denotes the complex-conjugate transpose of $\mathbf{A}$, i.e. $\mathbf{A}^* = (\overline{\mathbf{A}})'$.

Explicitly, all the 16 Mueller matrix components P_{ij} can be written as:

$$P_{11} = \frac{1}{2}(|S_1|^2 + |S_2|^2 + |S_3|^2 + |S_4|^2)$$

$$P_{12} = \frac{1}{2}(|S_2|^2 - |S_1|^2 + |S_4|^2 - |S_3|^2)$$

$$P_{13} = Re(S_2 S_3^* + S_1 S_4^*)$$

$$P_{14} = Im(S_2 S_3^* - S_1 S_4^*)$$

$$P_{21} = \frac{1}{2}(|S_2|^2 - |S_1|^2 - |S_4|^2 + |S_3|^2)$$

$$P_{22} = \frac{1}{2}(|S_2|^2 + |S_1|^2 - |S_4|^2 - |S_3|^2)$$

$$P_{23} = Re(S_2 S_3^* - S_1 S_4^*)$$

$$P_{24} = Im(S_2 S_3^* + S_1 S_4^*)$$

$$P_{31} = Re(S_2 S_4^* + S_1 S_3^*)$$

$$P_{32} = Re(S_2 S_4^* - S_1 S_3^*)$$

$$P_{33} = Re(S_1 S_2^* + S_3 S_4^*)$$

$$P_{34} = Im(S_2 S_1^* + S_4 S_3^*)$$

$$P_{41} = Im(S_2 S_4^* + S_3 S_1^*)$$

$$P_{42} = Im(S_2 S_4^* - S_3 S_1^*)$$

$$P_{43} = Im(S_1 S_2^* - S_3 S_4^*)$$

$$P_{44} = Re(S_1 S_2^* - S_3 S_4^*)$$

(2.20)

Therefore, the Mueller matrix contains all the scattering information of the scatterer and it only has 7 independent constants, same as the amplitude matrix. Then there must be 9 independent relations between these 16 elements [47].

14

2.4 Extinction, scattering and absorption

The concept of cross section is very useful to describe the total scattering effect of a scatterer. When a beam of light interacts with a scatterer, the energy is partly absorbed and partly scattered. The scattering, absorption and extinction cross sections are defined as the total scattered, absorbed, and extinguished monochromatic energy from the original beam divided by the monochromatic energy flux of the incident wave [44]. The Mueller matrix element P_{11}, also called the phase function, specifies the the angular distribution of the scattered light. The scattering cross section can be obtained by an integral of P_{11} over all directions:

$$C_{sca} = \frac{1}{k^2} \int_{\Omega} P_{11} d\Omega \tag{2.21}$$

The extinction can be obtained by the optical theorem:

$$C_{ext} = \frac{4\pi}{k^2 |\mathbf{E}^{inc}|^2} Re[(\mathbf{E}^{inc*} \cdot \mathbf{E}^{sca})_{\theta=0}] \tag{2.22}$$

This says extinction cross section is only determined by the exact forward scattering, which physically means the scatterer removes some energy by the interference between the forward scattered field and the incident field. Note for a general non-spherical particle, the extinction cross section will be different for different incident polarization states. In other words, we should have a extinction matrix to express the total removed power [14]. The absorption cross section will be the difference between the extinction cross section and the scattering cross section:

$$C_{abs} = C_{ext} - C_{sca} \tag{2.23}$$

And the single scattering albedo is defined as:

$$\omega_o = C_{sca}/C_{ext} \tag{2.24}$$

ω_o is bounded in (0,1], and $\omega_o = 0$ means no absorption.

3. SIMULATING THE UNDERWATER POLARIZED LIGHT FIELD USING A BACKWARD MONTE CARLO METHOD

3.1 Vector radiative transfer model

The radiative transfer (RT) model [13, 14] is a powerful method to solve the multiple scattering when the particulate medium is sparsely packed [14, 29], i.e. when the scatterings are assumed independent and no phase information is carried. The vector transfer equation (VRTE) can be written as [14]:

$$\hat{n} \cdot \nabla \mathbf{I}(\vec{r}, \hat{n}) = -\mathbf{K}(\vec{r}, \hat{n}) \, \mathbf{I}(\vec{r}, \hat{n}) + \int_{\Omega} \beta_s(\hat{n}') \mathbf{P}(\hat{n}', \hat{n}) \mathbf{I}(\vec{r}, \hat{n}') d\Omega(\hat{n}') \tag{3.1}$$

where ∇ is the divergence operator and $\hat{n} \cdot \nabla$ represents a directional derivative in direction $\hat{n}$, $\mathbf{I}(\vec{r}, \hat{n})$ is the Stokes vector defined in the meridian plane, $\mathbf{K}(\vec{r}, \hat{n})$ is the extinction coefficient matrix considering the extinction dependence of incident polarization states, and $\mathbf{P}(\hat{n}', \hat{n})$ is the phase matrix. Eq. (3.1) states there are two terms that contribute to the directional derivative of the Stokes vector. The first term represents the attenuation of the light field caused by extinction along the direction $\hat{n}$ and the second term represents the contribution of multiple scattered light from all directions into the current direction $\hat{n}$.

We can define the position and direction vector as:

$$\vec{r} = (x, y, z) \tag{3.2}$$

$$\hat{n} = (\sqrt{1 - \mu^2} \cos \phi, \sqrt{1 - \mu^2} \sin \phi, \mu) \tag{3.3}$$

Then the directional derivative can be expressed as:

$$\hat{n} \cdot \nabla \mathbf{I}(\vec{r}, \hat{n}) = \frac{d\mathbf{I}(\vec{r}, \hat{n})}{ds} = \mu \frac{d\mathbf{I}(\vec{r}, \hat{n})}{dz} \tag{3.4}$$

17

It is very convenient to define the Stokes vector $\mathbf{I} = (I, Q, U, V)^T$ in the meridian plane, which contains the z-axis of the laboratory frame of reference and the incident or scattered directions. However, the scattering Mueller matrix $\mathbf{P}_s(\hat{n}', \hat{n})$ is normally defined in the scattering plane, as shown in Figure 3.1. We need two rotations associated with the scattering Mueller matrix to obtain the phase matrix [13]:

$$\mathbf{P}(\hat{n}', \hat{n}) = \mathbf{L}(\pi - i_2)\mathbf{P}_s(\hat{n}', \hat{n})\mathbf{L}(-i_1) \tag{3.5}$$

where $\mathbf{L}(-i_1)$ rotates the reference plane from the initial meridian plan to the scattering plan, and $\mathbf{L}(\pi - i_2)$ rotates the reference plane from the scattering plane to the final meridian plan. Here the first component of the phase matrix, which is called phase function, is normalized so we can use it to sample the scattering angles:

$$\int_\Omega P_{11}(\hat{n}', \hat{n})d\Omega(\hat{n}') = 1 \tag{3.6}$$

The VRTE (Eq. (3.1)) is an ordinary differential equation (ODE). Its general integral solution can be written as:

$$\mathbf{I}(\vec{r}, \hat{n}) = \mathbf{T}(\vec{r}_m, \vec{r}, \hat{n})\mathbf{I}(\vec{r}_m, \hat{n}) + \int_{z_m}^{z} \frac{dz}{\mu}\mathbf{T}(\vec{r}', \vec{r}, \hat{n}) \int_{\Omega'} \beta_s(\hat{n}')\mathbf{P}(\hat{n}', \hat{n})\mathbf{I}(\vec{r}', \hat{n}')d\Omega(\hat{n}') \tag{3.7}$$

where $\mathbf{T}(\vec{r}', \vec{r}, \hat{n})$ is the transmission matrix from $\vec{r}'$ to $\vec{r}$ along the direction $\hat{n}$, which is defined as:

$$\mathbf{T}(\vec{r}', \vec{r}, \hat{n}) = \exp[-\mathbf{K}(\vec{r}', \hat{n})|\vec{r}' - \vec{r}|] \tag{3.8}$$

The general solution given by (Eq. (3.7)) is not an analytic solution. We will see later we can get the successive order solution based on the general solution.
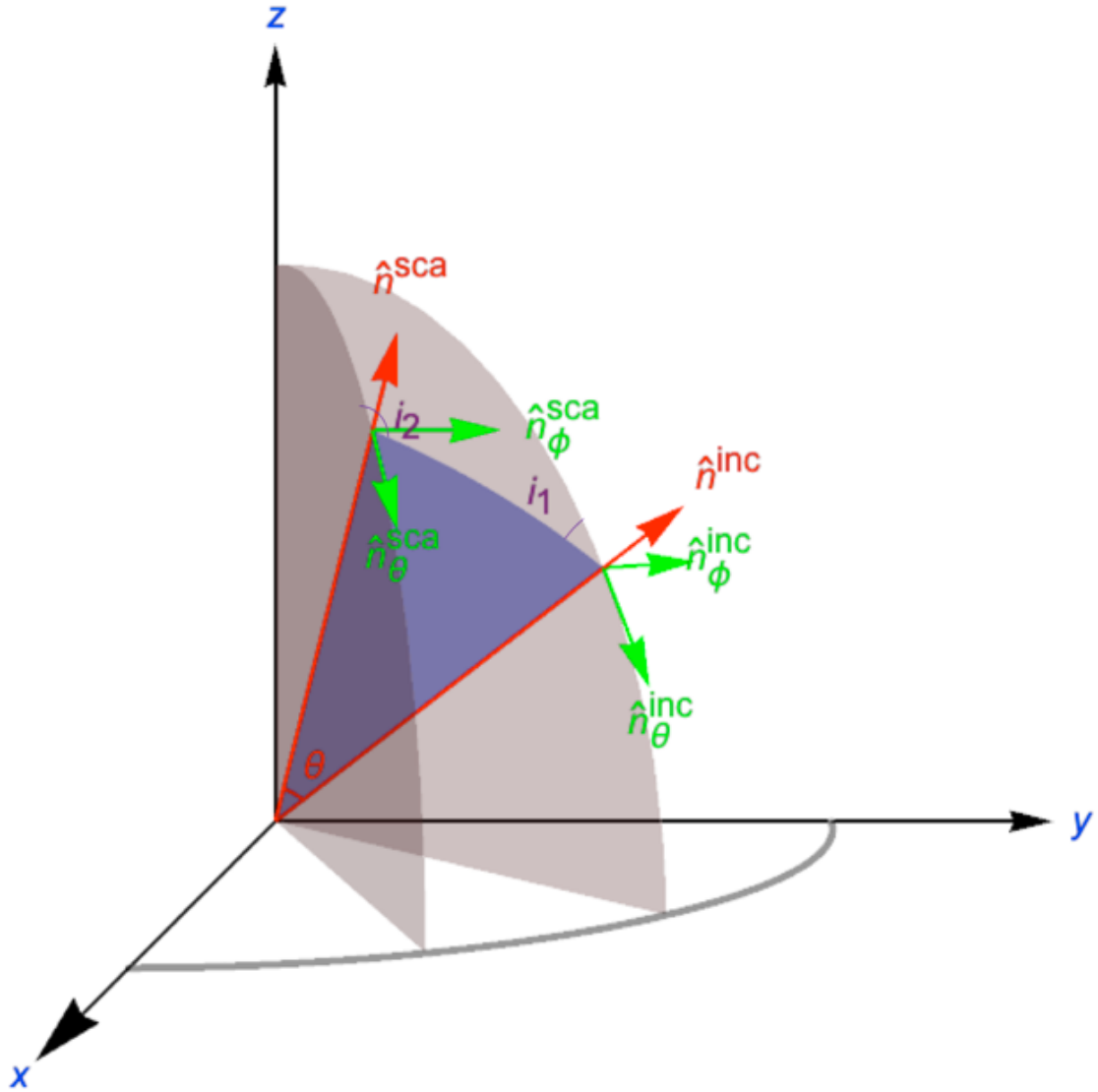
Figure 3.1: Rotation of the Stokes vectors. The scattering angle is θ in the scattering plane (indicated in blue). The Stokes vectors are defined in the meridian planes (indicated in pink) which contain the z-axis of the laboratory frame of reference and the incident or scattered directions. $\mathbf{L}(-i_1)$ rotates the reference plane from the initial meridian plan to the scattering plan, and $\mathbf{L}(\pi - i_2)$ rotates the reference plane from the scattering plane to the final meridian plan.

3.2 The successive orders of scattering (SOS) method

In the SOS model, the total Stokes vector can be expressed as the summation of all order of scattering terms:

$$\mathbf{I}(\vec{r}, \hat{n}) = \sum_{n=0}^{\infty} \mathbf{I}_n(\vec{r}, \hat{n}) \tag{3.9}$$

Since the VRTE is linear, we can introduce the effective Mueller matrix which relates the incident Stokes vector and the scattered Stokes vector:

$$\mathbf{I}(\vec{r}, \hat{n}) = \mathbf{M}^{eff}(\vec{r}, \hat{n})\mathbf{I}_0 \tag{3.10}$$

The effective Mueller matrix contains all the optical response properties of the medium. For arbitrary polarization states of the incident beam, we can immediately obtain the polarization states of the transmitted beam. Similarly, the total effective Mueller matrix can be expressed as the summation of effective Mueller matrix of all order of scattering terms:

$$\mathbf{M}^{eff}(\vec{r}, \hat{n}) = \sum_{n=0}^{\infty} \mathbf{M}_n^{eff}(\vec{r}, \hat{n}) \tag{3.11}$$

Based on (Eq. (3.7)), we can see that the n-th order term can be expressed iteratively in terms of the (n-1)-th order term:

$$\mathbf{M}_n^{eff}(\vec{r}, \hat{n}) = \int_{z_m}^{z} \frac{dz'}{\mu}\mathbf{T}(\vec{r}', \vec{r}, \hat{n}) \int_{\Omega'} \beta_s(\hat{n}')\mathbf{P}(\hat{n}', \hat{n})\mathbf{M}_{n-1}^{eff}(\vec{r}', \hat{n}')d\Omega(\hat{n}') \tag{3.12}$$

We may come back to have a careful look at the 0-th order term. For simplicity, we just consider a plane wave source at the boundary in the direction $\hat{n}_0$:

$$\mathbf{I}(\vec{r}_m, \hat{n}) = \mathbf{I}_0\delta(\hat{n} - \hat{n}_0) \tag{3.13}$$

Then the 0-th order effective Mueller matrix is just the attenuating term of the direct source:

$$\mathbf{M}_0^{eff}(\vec{r}, \hat{n}) = \mathbf{T}(\vec{r_m}, \vec{r}, \hat{n}_0)\delta(\hat{n} - \hat{n}_0) \qquad (3.14)$$

Then the first order

$$\mathbf{M}_1^{eff}(\vec{r}, \hat{n}) = \int_{z_m}^{z} \frac{dz_1}{\mu}\mathbf{T}(\vec{r_1}, \vec{r}, \hat{n})\beta_s(\hat{n}_0)\mathbf{P}(\hat{n}_0, \hat{n})\mathbf{T}(\vec{r_m}, \vec{r_1}, \hat{n}_0) \qquad (3.15)$$

With (Eq. (3.12)) and (Eq. (3.15)), iteratively we can obtain all order of scattering terms.

3.3 The Vector Monte Carlo method

Even though we have all the iterative terms of the SOS method, it's not practical to calculate them all analytically. For systems with randomly positioned and arbitrarily oriented particles, the extinction matrix reduces to the scalar case, and Monte Carlo method becomes a possible way to numerically solve the VRTE.

In the Monte Carlo model [18, 23, 24, 25], the scattering medium is statistically homogeneous in certain regions. Both the extinction coefficient matrix and the phase matrix are independent of the position. In other words, the probability to find a scatterer at any position in the medium is the same. We can statistically evaluate the integrations over the distances and solid angles in the SOS method by the summation over sampled distances and sampled scattering angles. We will see later, for each scattering event, the path length is distributed with an exponential probability density function and the scattering angle is distributed with the single scattering phase function. With the probability of each independent scattering event in a sequence of events known, we can obtain the statistical scattering estimate of the final outcome.

We start with the first order scattering term, which can be written in two forms:

$$\mathbf{M}_1^{eff}(\vec{r}, \hat{n}) = \int_{z_m}^{z} \frac{dz_1}{\mu} \mathbf{T}(\vec{r_1}, \vec{r}, \hat{n}) \beta_s(\hat{n}_0) \mathbf{P}(\hat{n}_0, \hat{n}) \mathbf{T}(\vec{r_m}, \vec{r_1}, \hat{n}_0) \qquad (3.16)$$

$$= \frac{\mu_0}{\mu} \int_{z_m}^{z} \frac{dz_1}{\mu_0} \mathbf{T}(\vec{r_1}, \vec{r}, \hat{n}) \beta_s(\hat{n}_0) \mathbf{P}(\hat{n}_0, \hat{n}) \mathbf{T}(\vec{r_m}, \vec{r_1}, \hat{n}_0) \qquad (3.17)$$

The two different forms represent two different sample directions: the forward Monte Carlo and the backward Monte Carlo. For first order scattering, the scattering angle is just the angle between $\hat{n}_0$ and $\hat{n}$, and what we need to do is just to sample the first scattering position. In (Eq. (3.17)), $\mathbf{T}(\vec{r_m}, \vec{r_1}, \hat{n}_0)$ represent the transmission from the boundary position $\vec{r_m}$ to the scattering position $\vec{r_1}$, therefore we can use it to sample a path-length z_1/μ_0 assuming the photon starts from the boundary point $\vec{r_m}$ and proporgates along $\hat{n}_0$. The left $\mathbf{T}(\vec{r_1}, \vec{r}, \hat{n}) \mathbf{P}(\hat{n}_0, \hat{n})$ represents the contribution of the scattering from the source direction $\hat{n}_0$ to the detector direction $\hat{n}$ and the transmission from the first scattering position $\vec{r_1}$ to the detector position $\vec{r}$.

Alternatively, we can sample the photon from the detector to the source. In (Eq. (3.16)), the transmission matrix from the scattering position $\vec{r_1}$ to the detector position $\vec{r}$ is $\mathbf{T}(\vec{r_1}, \vec{r}, \hat{n})$, which can be used to sample a pathlength z_1/μ assuming the photon starts from the detector position $\vec{r}$ and proporgates along $\hat{n}$. The left $\mathbf{P}(\hat{n}_0, \hat{n}) \mathbf{T}(\vec{r_m}, \vec{r_1}, \hat{n}_0)$ represents the contribution of the scattering from the source direction $\hat{n}_0$ to the detector direction $\hat{n}$ and the transmission from the first scattering point $\vec{r_1}$ to the boundary position $\vec{r_m}$. The difference with the forward Monte Carlo sampling is that we have no extra factor for the backward Monte Carlo sampling.

Similarly, based on the iterative equation (Eq. (3.12)), we can write the second order

scattering term in two forms:

$$\mathbf{M}_2^{eff}(\vec{r}, \hat{n}) = \int_{z_m}^{z} \frac{dz_2}{\mu} \mathbf{T}(\vec{r_2}, \vec{r}, \hat{n}) \int_{\Omega} d\Omega(\hat{n}_1) \beta_s(\hat{n}_1) \mathbf{P}(\hat{n}_1, \hat{n}) \tag{3.18}$$

$$\cdot \int_{z_m}^{z_2} \frac{dz_1}{\mu_1} \mathbf{T}(\vec{r_1}, \vec{r_2}, \hat{n}_1) \beta_s(\hat{n}_0) \mathbf{P}(\hat{n}_0, \hat{n}_1) \mathbf{T}(\vec{r_m}, \vec{r_1}, \hat{n}_0) \tag{3.19}$$

$$= \frac{\mu_0}{\mu} \int_{z_m}^{z} \frac{dz_2}{\mu_1} \mathbf{T}(\vec{r_2}, \vec{r}, \hat{n}) \int_{\Omega} d\Omega(\hat{n}_1) \beta_s(\hat{n}_1) \mathbf{P}(\hat{n}_1, \hat{n}) \tag{3.20}$$

$$\cdot \int_{z_m}^{z} \frac{dz_1}{\mu_0} \mathbf{T}(\vec{r_1}, \vec{r_2}, \hat{n}_1) \beta_s(\hat{n}_0) \mathbf{P}(\hat{n}_0, \hat{n}_1) \mathbf{T}(\vec{r_m}, \vec{r_1}, \hat{n}_0) \tag{3.21}$$

Again we have two different sampling directions based on the two different forms. Eq. (3.21) illustrates the forward Monte Carlo sampling. $\mathbf{T}(\vec{r_m}, \vec{r_1}, \hat{n}_0)$ represents the transmission from the boundary position $\vec{r_m}$ to the first scattering position $\vec{r_1}$, thus we can use it to sample the first photon path-length z_1/μ_0 assuming the photon starts from the boundary point $\vec{r_m}$ and proporgates along $\hat{n}_0$. Then $\mathbf{P}(\hat{n}_0, \hat{n}_1)$ represents the first scattering from the source direction $\hat{n}_0$ to the scattering direction $\hat{n}_1$, which can be used to sample the first scattering direction $\hat{n}_1$. The transmission matrix $\mathbf{T}(\vec{r_1}, \vec{r_2}, \hat{n}_1)$ represents the transmission from the first scattering position $\vec{r_1}$ to the second scattering position $\vec{r_2}$, which then can be used to sample the second scattering position $\vec{r_2}$. At last, the left estimation part $\mathbf{T}(\vec{r_2}, \vec{r}, \hat{n}) \mathbf{P}(\hat{n}_1, \hat{n})$ represents the multiplication of the scattering from the first scattering direction $\hat{n}_1$ to the detector direction $\hat{n}$ and the transmission from the second scattering point $\vec{r_2}$ to the detector position $\vec{r}$.

While Eq. (3.19) illustrates the backward Monte Carlo sampling. First we use $\mathbf{T}(\vec{r_2}, \vec{r}, \hat{n})$ to sample a photon path-length z_2/μ assuming the photon starts from the detector position $\vec{r}$ and propagates along $\hat{n}$. Then we use $\mathbf{P}(\hat{n}_1, \hat{n})$ to sample the new propagating direction $\hat{n}_1$ after the first scattering. Now our photon is at position $\vec{r_2}$ and propagates along $-\hat{n}_1$, we then use $\mathbf{T}(\vec{r_1}, \vec{r_2}, \hat{n}_1)$ to sample a photon path-length z_1/μ_1 to make it proporgetes to another scattering position $\vec{r_1}$. At lat, the left $\mathbf{P}(\hat{n}, \hat{n}_0) \mathbf{T}(\vec{r_m}, \vec{r_1}, \hat{n}_0)$ represents the multi-

plication of the scattering from the source direction $\hat{n}_0$ to the detector direction $\hat{n}$ and the transmission from the first scattering point $\vec{r_1}$ to the boundary position $\vec{r_m}$.

Continuing this iterative process based on equation Eq. (3.12), we can get the numerical estimation of all order of the scattering terms. Note the difference of the forward and backward Monte Carlo simulations is that the forward sampling will always leave us a μ_0/μ factor. For different circumstances, using symmetries we can simplify our iterative equation Eq. (3.12), which can greatly simplify our numerical sampling. We can also use some forced collision tricks and estimation methods to improve our sampling efficiency. We will talk about this more in the coming underwater simulation section.

3.4 Simulating the underwater polarized light field using a backward Monte Carlo method

The polarization nature of ocean light provides a diversity of applications such as marine biology, remote sensing and underwater imaging. Marine animals are able to use polarization to forage, to navigate and to communicate. The polarization properties of light in the ocean can also be used to improve underwater imaging image qualities. When modeling the atmosphere-ocean system, a good assumption is to simplify our problem and assumes scattering medium is statistically homogeneous in certain regions. This means both the extinction coefficient matrix and the phase matrix are independent of the position. In other words, the probability of finding a scatterer at any position in the medium in certain regions is the same. Thus we can use using a backward Monte Carlo method to statistically evaluate the underwater polarized light field.

We simulate the underwater light properties by propagating photons throughout the atmosphere-ocean system. Every photon we inject into the medium carries a weight ω and effective Mueller matrix $\mathbf{M}_p$. The weight represents the energy the photon currently carries and its initial value is 1.0. The effective Mueller matrix carries all the polarization

24

informations and it's a 4×4 identity matrix at the starting point. We will see later, for each scattering event, the path length is sampled based on the transmission matrix and the scattering angle is sampled based on the single scattering phase function. After each sampled scattering event, both the weight and the effective Mueller matrix of the photon will be updated. The photon will be terminated after its weight is smaller than some certain truncation value. We keep injecting photons and repeating this sampling process, the effective Mueller Matrix of the medium can be obtained from the statistical average result of a large number of photons.

In the atmosphere and in the ocean, the transmission matrix $\mathbf{T}(\vec{r_1}, \vec{r_2}, \hat{n})$ from $\vec{r_1}$ to $\vec{r_2}$ along the direction $\hat{n}$ reduces to the scalar case:

$$\mathbf{T}(\vec{r_1}, \vec{r_2}, \hat{n}) = T(\vec{r_1}, \vec{r_2}, \hat{n}) \, \mathbf{E}; \tag{3.22}$$

$$T(\vec{r_1}, \vec{r_2}, \hat{n}) = \exp(-\beta_{ext}|\vec{r_1} - \vec{r_2}|) \tag{3.23}$$

where $\mathbf{E}$ is a 4×4 identity matrix and β_{ext} is the extinction coefficient. Eq. 3.23 is just the Bouger-Lambert-Beer law, which states the transmission is the ratio of the original photon packet due to the attenuation. We can define the optical depth or the optical thickness between two points $\vec{r_1}$ and $\vec{r_2}$ as:

$$\tau = \beta_{ext}|\vec{r_1} - \vec{r_2}| \tag{3.24}$$

Then the transmission of the Bouger-Lambert-Beer law is simply:

$$T(\vec{r_1}, \vec{r_2}, \hat{n}) = e^{-\tau} \tag{3.25}$$

The fundamental principle of Monte Carlo calculation is to sample the variable based

25

on its probability density function. For example, we can sample the optical depth by

$$\int_0^\tau e^{-\tau} d\tau = \xi \tag{3.26}$$

where ξ is a random number which is uniformly distributed on $0 < \xi < 1$. Then we have

$$\tau = -\ln(1 - \xi) \tag{3.27}$$

Since $(1 - \xi)$ is another random number also uniformly distributed over the interval $(0,1)$, we can just use:

$$\tau = -\ln \xi \tag{3.28}$$

The sampled optical depth τ ranges from 0 to infinity. Obviously, this is not efficient since samplings of τ beyond the boundary, which means the photon will escape from the medium, will be discarded. Instead, we can use a so-call forced collision method. If the optical thickness along the current propagation direction is τ_m, as as shown in Figure 3.2, the fraction of photons that will escape from the medium without scattering will be $e^{-\tau_m}$. Thus we can force a collision over the optical depth interval $(0,\tau_m)$ by using the weighted sampling:

$$\frac{\int_0^\tau e^{-\tau} d\tau}{\int_0^{\tau_m} e^{-\tau} d\tau} = \xi \tag{3.29}$$

which leaves us

$$\tau = -\ln(1 - (1 - e^{-\tau_m})\xi) \tag{3.30}$$

This will increase the sampling efficiency intensively, especially for a thin scattering medium. To remove the bias introduced by the weighted forced collision sampling, we
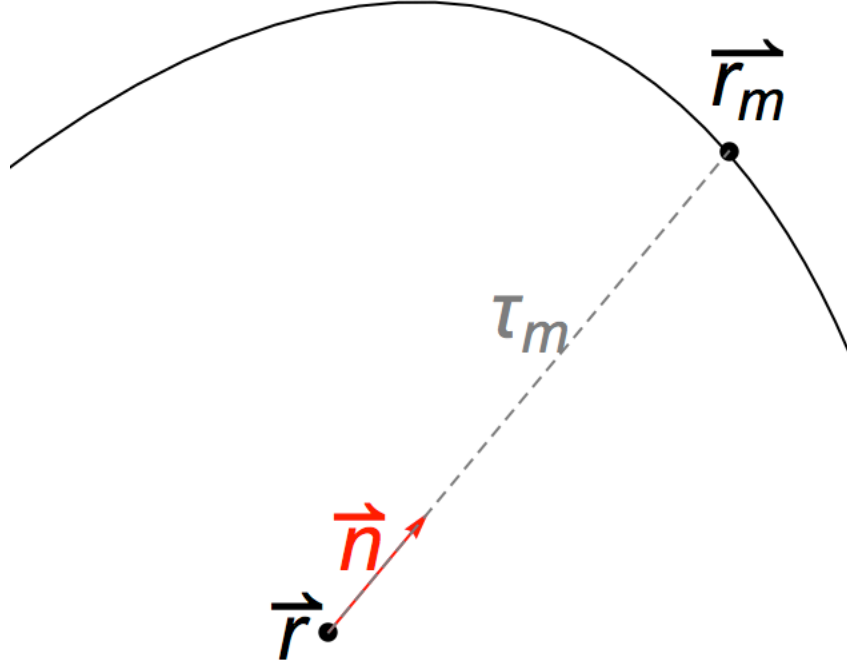
Figure 3.2: A diagram of a forced collision. The optical thickness along the current propagation direction is τ_m and our forced collision will be over the optical depth interval $(0, \tau_m)$.

need to multiply the photon weight by a weight factor:

$$\omega_2 = \omega_1(1 - e^{-\tau_m}) \tag{3.31}$$

where ω_1 and ω_2 are the initial and final weights, respectively. The physical meaning of the factor is the fraction of the photons that remain in the medium. After an optical depth is sampled, we can update the location of the photon;

$$\vec{r_2} = \vec{r_1} + \frac{\tau}{\beta_s} \cdot \hat{n} \tag{3.32}$$

where $\vec{r_1}$ and $\vec{r_2}$ are the initial and final positions, respectively, and $\hat{n}$ is the propagation

27

direction.

When the photon packet arrives to a new location, it will be scattered at some scattering angle. The scattering angle is determined by the single scattering phase function:

$$\int_{\Omega} P_{11}(\hat{n}, \hat{n}')d\Omega(\hat{n}') = 1 \tag{3.33}$$

For most cases, the phase function is independent of the azimuthal angle ϕ:

$$p(\theta, \phi) = p(\theta) \tag{3.34}$$

Thus we can separately sample the zenith angle θ (or $\mu = \cos\theta$) and the azimuthal angle by:

$$\xi_1 = 2\pi \int_{-1}^{u} p(\mu)d\mu, \tag{3.35}$$

$$\xi_2 = \int_{0}^{\phi} \frac{1}{2\pi}d\phi \tag{3.36}$$

where ξ_1 and ξ_2 are two independent random variables uniformly distributed over the interval (0,1). The the zenith angle θ (or $\mu = \cos\theta$) and the azimuthal angle can be obtained in terms of ξ_1 and ξ_2.

Two kinds of phase functions have been widely used due to their analytic mathematical simplicity. The first one is the phase function of Rayleigh scattering [45]. Rayleigh scattering is caused by particles much smaller than the wavelength of the radiation and the scattering in the atmosphere is dominated by this type of scattering. Therefore the Rayleigh phase function is often used to simulate the radiative transfer process in the atmosphere. Rayleigh scattering has the phase function and reduced Mueller matrix as

follows:

$$p_R(\theta) = \frac{3}{16\pi}(1 + \cos^2 \theta) \tag{3.37}$$

$$\mathbf{M}(\theta) = \begin{pmatrix} 1 & -\frac{\sin^2 \theta}{1+\cos^2 \theta} & 0 & 0 \\ -\frac{\sin^2 \theta}{1+\cos^2 \theta} & 1 & 0 & 0 \\ 0 & 0 & \frac{2\cos \theta}{1+\cos^2 \theta} & 0 \\ 0 & 0 & 0 & \frac{2\cos \theta}{1+\cos^2 \theta} \end{pmatrix} \tag{3.38}$$

Substitute Eq. (3.37) into Eq. (3.35) and Eq. (3.36) and we have the sampled scattering angle for the Rayleigh phase function:

$$\mu = (z + \sqrt{z^2 + 1})^{1/3} + (z - \sqrt{z^2 + 1})^{1/3}, \; where \; z = 2(2\xi_1 - 1) \tag{3.39}$$

$$\phi = 2\pi\xi_2 \tag{3.40}$$

Another widely used analytic phase function which is mainly used in ocean optics is the Henyey-Greenstein (HG) phase function [48]:

$$p_{HG}(\theta) = \frac{1}{4\pi}\frac{1 - g^2}{(1 + g^2 - 2g\cos \theta)^{3/2}} \tag{3.41}$$

where g is the asymmetry factor defined by

$$g = \int_{-1}^{1} \int_{0}^{2\pi} p(\theta, \phi) \cos \theta \sin \theta d\theta d\phi \tag{3.42}$$

Substituting Eq. (3.41) into Eq. (3.35) and Eq. (3.36), the scattering angle sampling for

HG phase function can be obtained:

$$\mu = \frac{1}{2g}(1 + g^2 - (\frac{1 - g^2}{1 + g(2\xi_1 - 1)})^2)$$ (3.43)

$$\phi = 2\pi\xi_2$$ (3.44)

Since the particles in the ocean are mainly soft particles which have a refractive index close to unity, the reduced scattering Mueller matrices of them are also Rayleigh like, which is as expressed in Eq. (3.38).

The two analytic phase functions can approximate the light scattering properties in the atmosphere and in the ocean water, respectively. However, discrepancies between the analytic result and real case can always be anticipated. What we will mainly use in our model is the phase function measured from the real ocean water in Curacao by Dr Alex Gilerson's group from City College of New York. The measured data, which has an asymmetry factor g=0.925, is compared with HG phase function, as plotted in Figure 3.3. It has very similar behavior with HG phase function with g=0.93, except a higher tail near the backward directions. Again, we will assume the reduced scattering Mueller matrix is Rayleigh like as expressed in Eq. (3.38). By substituting the numerical values of the phase function into Eq. (3.35) and Eq. (3.36), the scattering angle can be sampled. After the scattering angles are sampled, we can update our photon packet propagation direction based on the old propagation direction.

We have discussed how to sample the path length and scattering angle. In our model, we will use another trick, the so-called statistical estimation approach, to increase the simulation efficiency. This means, after each collision, we make an estimation to the source from the current position of the photon packet, which carries a weight w and an effective Mueller matrix $\mathbf{M}_p$. In this way, one photon packet will represent N photon trajectories after N times of collisions. Now we will explain how to calculate the statistical
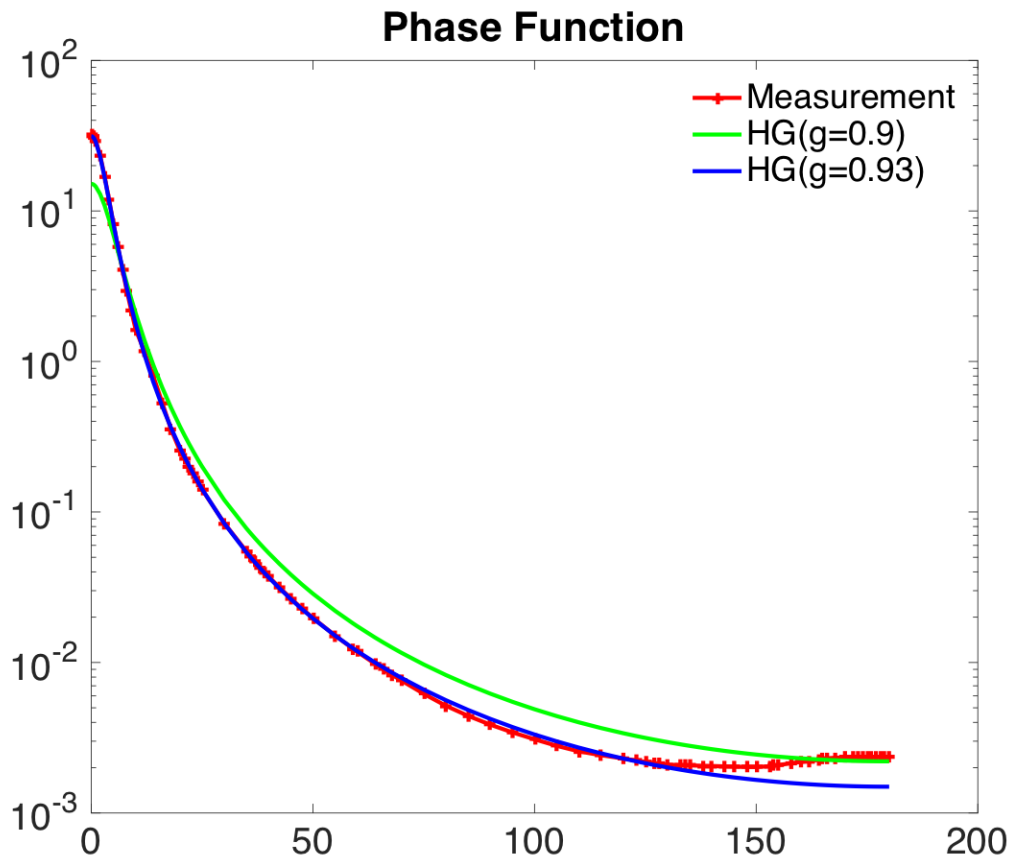
Figure 3.3: The measured phase function compared with HG phase function. The phase function (red dots) is measured in Curacao by Dr Alex Gilerson's Group from City College of New York. It has an asymmetry factor of 0.925.

estimation to the source for different cases.

3.4.1 Collision in the medium

We should make some updates and make an estimation to the source after each scattering event has happened. In the 3D case, the updates and estimation will depend on both the position and propagation direction of our current photon. Suppose the current photon carries a weight w and effective Mueller matrix $\mathbf{M}_p$ and propagates along $\hat{n}$. We will first update the photon weight by multiplying by the single scattering albedo ω_o:

$$w = w\omega_o \tag{3.45}$$

Physically, this accounts for that a fraction of $1 - \omega_o$ of the original photon packet will be removed due to absorption by the medium. If the photon is in the atmosphere layer, the estimation to the source can be expressed by:

$$\mathbf{M}_j = w \, exp(-\tau_s)\mathbf{M}_p\mathbf{L}(\pi - i_2)\mathbf{P}(\theta_s)\mathbf{L}(-i_1) \tag{3.46}$$

where τ_s is the optical distance between the current location and the boundary location at the atmosphere top traced back along the inverse source direction; θ_s is the scattering angle from the source direction to the current photon propagation direction, and $\mathbf{P}(\theta_s)$ is the Rayleigh Mueller matrix with scattering angle θ_s; $\mathbf{L}(-i_1)$ and $\mathbf{L}(\pi - i_2)$ are the two rotation matrix for scattering from the source direction to the current photon propagation direction. Note the orders of these matrix multiplication from the view of backward Monte Carlo method. In addition, we don't have the factor $1/\mu$, which is introduced only for forward Monte Carlo method.

When the collision point is in the ocean, we need two steps to make the estimation to the source. Given the current position and propagation direction as well as the source

direction, we can trace back the only trajectory for the photon packet. The photon will start from the current point to a point $\vec{r}_i$ in the atmosphere-ocean interface with scattering angle θ_s along a direction $\hat{n}_t$, then it goes from $\vec{r}_i$ to boundary point $\vec{r}_s$ at the atmosphere top along the inverse source direction. Thus the estimation can be written as the multiplication of the two steps:

$$\mathbf{M}_j = w\, exp(-\tau_i)\mathbf{M}_p\mathbf{L}(\pi - i_2)\mathbf{P}(\theta_s)\mathbf{L}(-i_1)$$
$$\cdot\, n^2 exp(-\tau_s)\mathbf{L}(\pi - i_2')\mathbf{T}(\theta_i)\mathbf{L}(-i_1') \tag{3.47}$$

where the first line represents the scattering in the water, τ_i is the optical distance between current point and point $\vec{r}_i$, $\mathbf{P}(\theta_s)$ is the scattering Mueller matrix with scattering angle θ_s, and $\mathbf{L}(-i_1)$ and $\mathbf{L}(\pi - i_2)$ are the two rotation matrices for scattering from direction $\hat{n}_t$ to the current photon propagation direction; the second line represents the transmission through the interface, τ_s is the optical distance between point $\vec{r}_i$ and point $\vec{r}_s$, $\mathbf{T}(\theta_i)$ is the transmission Mueller matrix with incident angle θ_i, and $\mathbf{L}(-i_1')$ and $\mathbf{L}(\pi - i_2')$ are the two rotation matrices for scattering from the source direction to the direction $\hat{n}_t$. n^2 here is the n^2 law for radiance [49] caused by transmission on the boundary from medium 1 to medium 2, where n is the refractive index of medium 2 relative to medium 1.

What's more, after a new scattering direction is sampled, we need to update the effective Mueller matrix carried by the photon packet:

$$\mathbf{M}_p = \mathbf{M}_p\mathbf{L}(\pi - i_2)\tilde{\mathbf{P}}(\theta_s)\mathbf{L}(-i_1)$$
$$= \mathbf{M}_p\mathbf{L}(\pi - i_2)\frac{\mathbf{P}(\theta_s)}{p(\theta_s)}\mathbf{L}(-i_1) \tag{3.48}$$

where $\tilde{\mathbf{P}}(\theta_s)$ is the reduced scattering matrix, $\mathbf{L}(-i_1')$ and $\mathbf{L}(\pi - i_2')$ are the two rotation matrices for scattering from the inverse new propagation direction to the inverse old propagation direction.

For the following two types of collisions, we only need to replace the phase matrices in

Eq. (3.46), Eq. (3.47) and Eq. (3.48) by their specific phase matrices to make the estimation or update.

3.4.2 Lambertian reflection

The photon will encounter some surfaces with Lambertian reflection, such as the ocean bottom or the spheres with a Lambertian surface. The Lambertian reflection means the reflected radiance will be isotropic, i.e. the radiance of a Lambertian surface is the same regardless of the observer's angle of view. The phase matrix of this kind of surface is:

$$p_L(\theta) = \frac{\cos\theta}{\pi} \tag{3.49}$$

$$\mathbf{M}(\theta) = \begin{pmatrix} 1 & 0 & 0 & 0 \\ 0 & 0 & 0 & 0 \\ 0 & 0 & 0 & 0 \\ 0 & 0 & 0 & 0 \end{pmatrix} \tag{3.50}$$

Substitute Eq. (3.49) into Eq. (3.35) and Eq. (3.36), we have the sampled scattering angle for a Lambertian scattering:

$$\mu = \sqrt{\xi_1} \tag{3.51}$$

$$\phi = 2\pi\xi_2 \tag{3.52}$$

3.4.3 Fresnel reflection

When the photon hits the atmosphere-ocean interface, the surrounding glass wall or the mirror spheres, the scattering matrix will be dominated by Fresnel's law [44]. For the mirror reflection surfaces, we can treat the surface as a medium with imaginary refractive index, such as silver. For an incident angle θ_i from medium 1 to medium 2, the Fresnel's

law reads:

$$\sin \theta_i = n \sin \theta_t \tag{3.53}$$

where θ_t is the transmitted angle and n is the refractive index of medium 2 relative to medium 1. The reflection and transmission coefficients for the parallel and perpendicular components are:

$$r_l = \frac{\cos \theta_t - n \cos \theta_i}{\cos \theta_t + n \cos \theta_i} \tag{3.54}$$

$$r_r = \frac{\cos \theta_i - n \cos \theta_t}{\cos \theta_i + n \cos \theta_t} \tag{3.55}$$

$$t_l = \frac{2 \cos \theta_i}{\cos \theta_t + n \cos \theta_i} \tag{3.56}$$

$$t_r = \frac{2 \cos \theta_i}{\cos \theta_i + n \cos \theta_t} \tag{3.57}$$

Then the reflection and transmission Mueller matrix from the Fresnel's law for the wave vectors can be expressed as:

$$\mathbf{R} = \begin{pmatrix} \frac{1}{2}(|r_l|^2 + |r_r|^2) & \frac{1}{2}(|r_l|^2 - |r_r|^2) & 0 & 0 \\ \frac{1}{2}(|r_l|^2 - |r_r|^2) & \frac{1}{2}(|r_l|^2 + |r_r|^2) & 0 & 0 \\ 0 & 0 & Re(r_l r_r^*) & Im(r_l r_r^*) \\ 0 & 0 & Im(r_l r_r^*) & Re(r_l r_r^*) \end{pmatrix} \tag{3.58}$$

$$\mathbf{T} = \begin{pmatrix} \frac{1}{2}(|t_l|^2 + |t_r|^2) & \frac{1}{2}(|t_l|^2 - |t_r|^2) & 0 & 0 \\ \frac{1}{2}(|t_l|^2 - |t_r|^2) & \frac{1}{2}(|t_l|^2 + |t_r|^2) & 0 & 0 \\ 0 & 0 & Re(t_l t_r^*) & Im(t_l t_r^*) \\ 0 & 0 & Im(t_l t_r^*) & Re(t_l t_r^*) \end{pmatrix} \tag{3.59}$$

The element R_{11} is the reflectivity, which is the probability that the beam gets reflected. Therefore we can use a random number ξ which again is uniformly distributed over the

interval (0,1), to compare with the reflectivity to decide if the photon packet is reflected or transmitted after it hits the surface: if $\xi < R_{11}$, the photon is reflected; otherwise it is transmitted. Note that for total internal reflection or reflection by medium with imaginary refractive index, the R_{43} element will be nonzero. This will produce circular polarization, and we will see this in later simulation results.
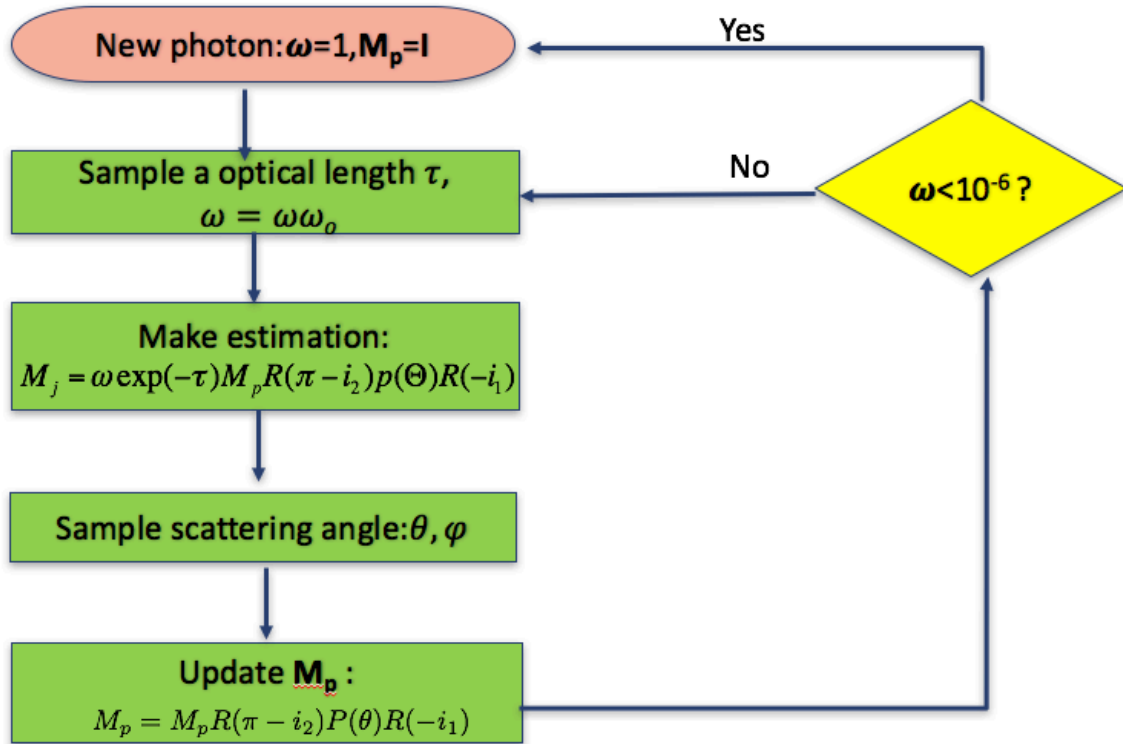
Figure 3.4: The flowchart of the backward Monte Carlo simulation procedure.

In summary, the basic procedure of the backward Monte Carlo simulation is as shown in Figure 3.4. Initially, we inject a new photon with $w = 1$ and effective Mueller matrix $\mathbf{M}_p = \mathbf{I}$. An optical length is sampled according to Eq. (3.30) to get the new collision point. Then estimation to the source is made by Eq. (3.46) or Eq. (3.47). A scattering

36

angle is sampled by Eq. (3.35) and Eq. (3.36) to find the new propagation direction. Then we update our photon effective Mueller matrix $\mathbf{M}_p$ according to Eq. (3.48). Now we test the current photon weight ω to decide if we continue the sampling or terminate the current photon. If the current photon weight ω is small enough, we terminate the photon and inject a new photon to repeat the whole process. A sampling example is illustrated as in Figure 3.5. We have three scattering events (two in the ocean and one in the atmosphre) before the photon is killed. Using the statistical estimation approach, we actually have three photon trajectories which all make the contribution to final result, even though only one photon is shot.
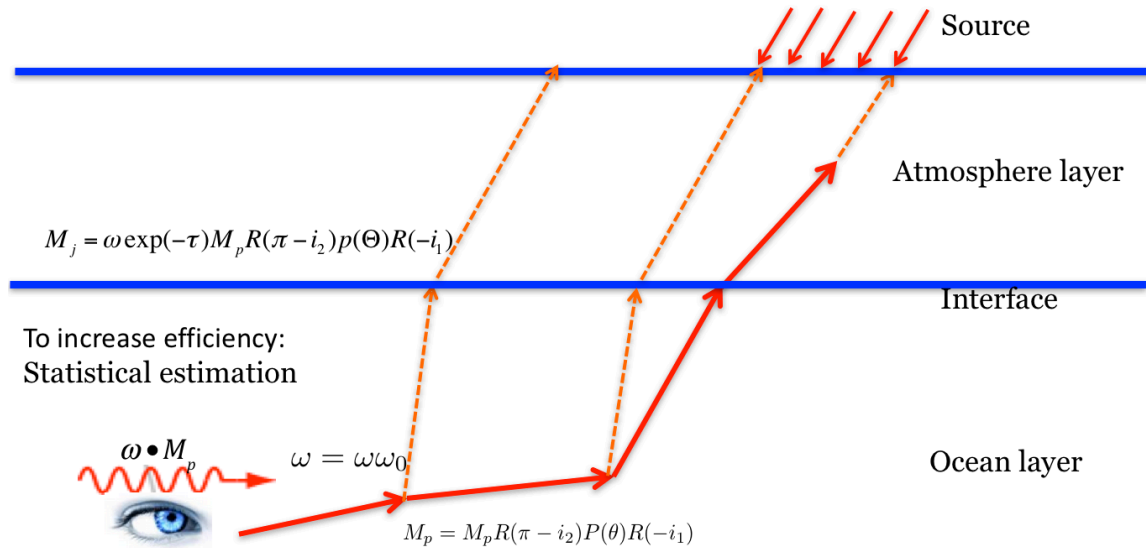
Figure 3.5: An example to illustrate the backward Monte Carlo simulation for one photon. The three scatterings provide three photon trajectories which all make the contribution to final result, even though only one photon is shot.

3.5 Result

3.5.1 Validation
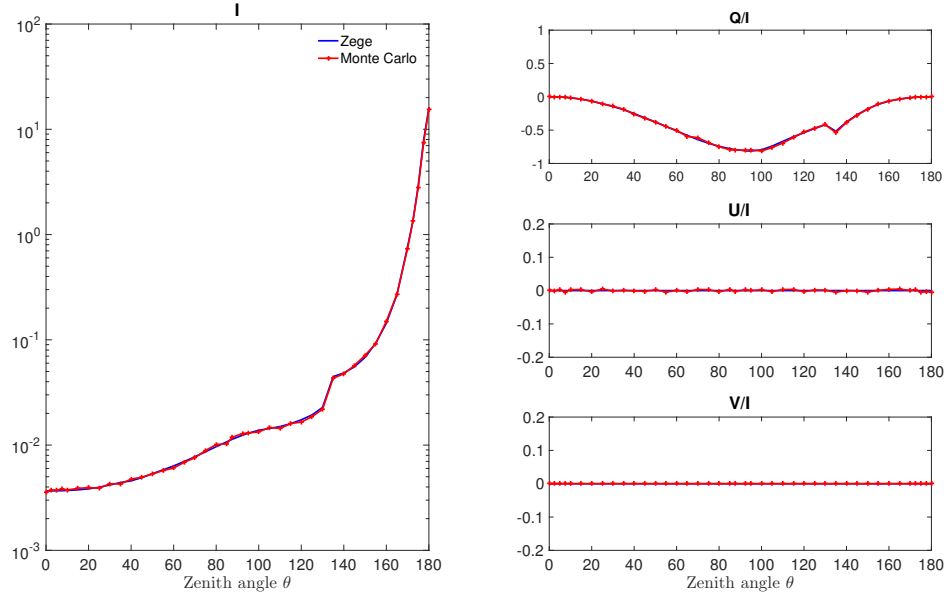
Figure 3.6: Comparison between the backward Monte Carlo and Zege's code calculations for an plane-parallel atmosphere-ocean system. The atmosphere layer has an optical depth of 0.15 with Rayleigh scattering (single scattering albedo 1.0) and the ocean layer has an optical depth of 10.0 with HG phase scattering (single scattering albedo 0.85) with asymmetry factor g=0.93. The detector is placed at a point with optical depth of 1.0 under the interface.

We have introduced a backward Monte Carlo method to calculate the 3D vector radiation field for the atmosphere-ocean system. This model can deal with a dynamic interface, different boundary conditions and complex ocean environments. To validate our code, we compared our results with the benchmark results by Zege's code [50] for a plane-parallel atmosphere-ocean system. We assume the atmosphere layer has an optical depth of 0.15 with Rayleigh scattering and the ocean layer has an optical depth of 10.0 with HG phase

scattering with asymmetry factor g=0.93. The detector is placed at a point with optical depth of 1.0 under the interface. In Figure 3.6, we show a comparison of the four Stokes vector elements between the two methods. The agreement is always within a few percent for all components. We have almost the same jumping behavior near the Snell's window (zenith angle near 132°) for both I and Q components. Our Monte Carlo code can accurately predict the Mueller matrix elements for different scattering angles.

3.5.2 Tank model
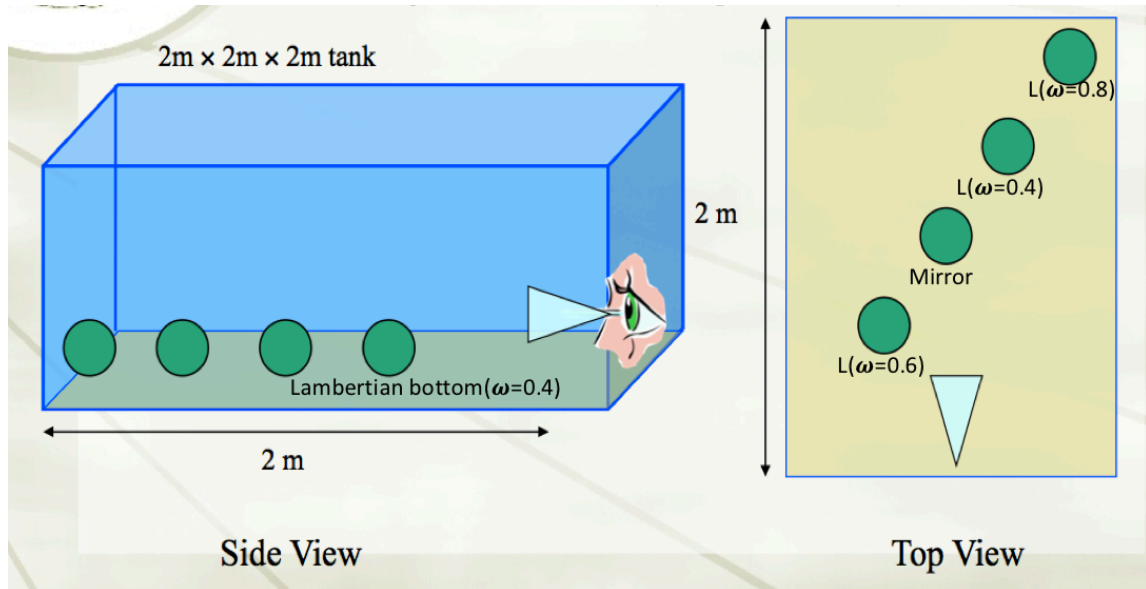
Figure 3.7: Illustration of the modeling of a detector. The tank has surrounding glass walls with refractive index 1.5 and a Lambertian bottom with albedo $\omega_b = 0.4$. Several spheres with different sizes and different scattering properties are put along the diagonal in the tank.

Marine animals are capable of detecting light polarization in the ocean. Many experiments about these marine animals are made in a tank rather than in the open ocean. This may bring in some artifacts because these marine animals in the tank may see differently

39

from what they see in the open ocean. To account for this, we first use a tank model,which is illustrated in Figure 3.7, to simulate what a marine organism can see under the water. The tank has surrounding glass walls with refractive index 1.5 and a Lambertian bottom with albedo $\omega_b = 0.4$. Several spheres with different sizes and different scattering properties are placed along the diagonal in the tank. We can simulate different underwater circumstances by changing the following parameters: the incident light direction, the way light scatters (phase function), the absorption and extinction coefficient, viewing position and viewing direction, and so on.
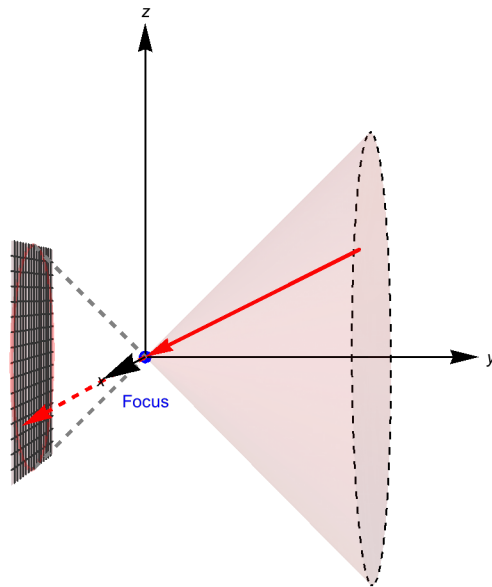
Figure 3.8: Illustration of the modeling of a detector. The screen is divided into many pixels, and each pixel corresponds to a different direction along which photons can hit the pixel through the focus point. After we collect the light information of all the pixels, the image of the viewing cone can be obtained.

A simulation of the way how cameras or human eyes work to get the image information inside the viewing cone, as shown in Figure 3.8, is needed to get the underwater image. The screen is divided into many small pixels, and each pixel corresponds to a different direction along which photons can hit the pixel through the focus point. After we collect the light information of all the pixels, the image of the viewing cone can be obtained. In our backward Monte Carlo model, we send photons from the detector and make estimations to the source. For each pixel in the screen array, we first calculate its corresponding direction and then shoot photons at the detector position along the corresponding direction. Effective Mueller matrices are obtained for all directions, thus all the Mueller matrices information for our image is obtained. We can change the detector position, its viewing directions as well as the angles of the viewing cone. In such a way, we can get the Mueller matrix image information at any points along any viewing directions inside the atmosphere-ocean system. Having the effective Mueller Matrix, we can obtain the Stokes vector(I,Q,U,V) as well as the degree of polarization (DOP), which compose all the polarization information.

In the tank model, we assume the atmosphere layer has an optical depth of 0.15 with Rayleigh scattering (single scattering albedo 1.0), which is the characteristic of the earth's atmosphere. Inside the ocean, light scattering has HG phase function (single scattering albedo 0.85) with asymmetry factor g=0.93 and Rayleigh type reduced Mueller matrix. The optical depth between the ocean surface and the spheres is 2.0. The four components of the Stokes vector for this case are shown in Figure 3.9, assuming the unpolarized sunlight is normal incident. From the radiance image, we can see clearly the four balls as well as their shadows on the Lambertian bottom. The individual Lambertian sphere displays isotropic brightness, while a lower reflection albedo will result in a dimmer image. There is a bright spot on the top of the mirror sphere due to the specular reflection of the directly incident sunlight. It's fascinating we have the image of the surrounding objects on the

41
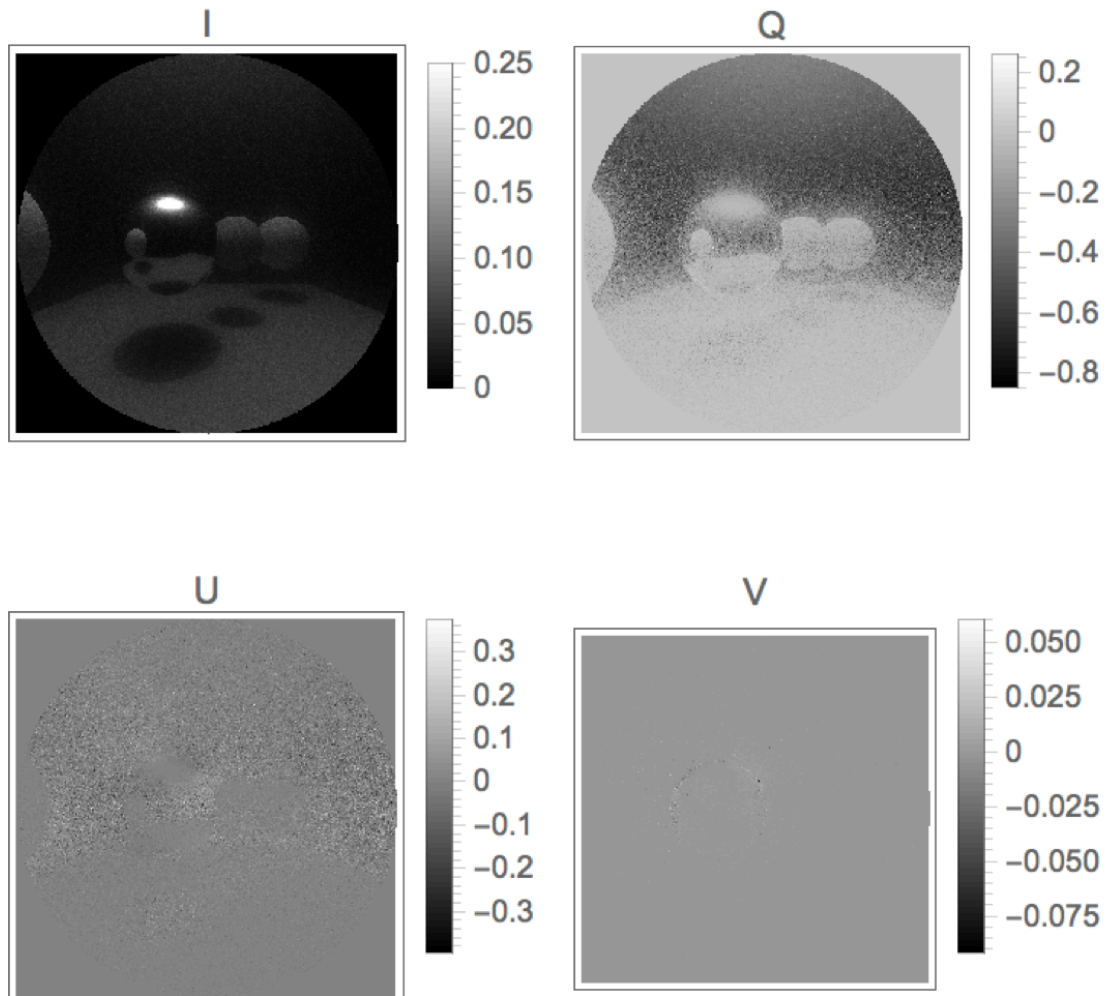
Figure 3.9: Underwater images of the four components of the Stokes vector, when the optical depth between the ocean surface and the spheres is 2.0. We assume the atmosphere layer has an optical depth of 0.15 with Rayleigh scattering (single scattering albedo 1.0), which is the characteristic of the earth's atmosphere. Inside the ocean, light scattering has HG phase function (single scattering albedo 0.85) with asymmetry factor g=0.93 and Rayleigh type reduced Mueller matrix.
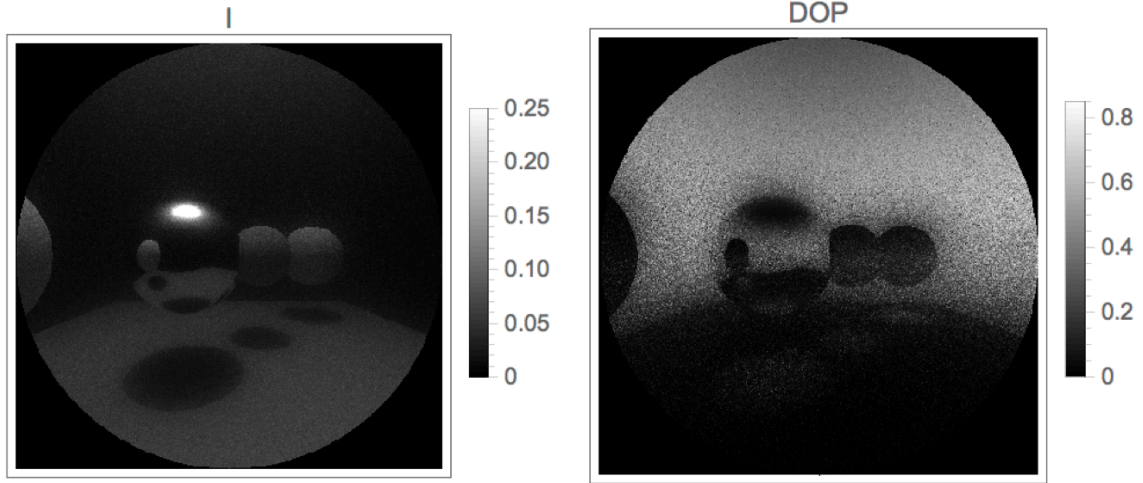
Figure 3.10: Underwater images of radiance and DOP, when the optical depth between the ocean surface and the spheres is 2.0. We assume the atmosphere layer has an optical depth of 0.15 with Rayleigh scattering (single scattering albedo 1.0), which is the characteristic of the earth's atmosphere. Inside the ocean, light scattering has HG phase function (single scattering albedo 0.85) with asymmetry factor g=0.93 and Rayleigh type reduced Mueller matrix.

mirror sphere surface, just as in the real life. The surrounding glass walls are quite black since we assume all the transmitted photons are absorbed to simplify our model. From the Q components, we can only see very blur images of the four spheres and the bottom without too much details. U components tell us very litter information about system even though they have considerable amplitude. The V components, which represents circular polarization, are always very small since Rayleigh typed reduced Mueller matrix scattering couldn't produce circular polarization. As we mentioned previously, circular polarization can only be caused by total internal reflection and mirror reflection as the Mueller matrix element M_{43} is nonzero.

Since Q, U and V components carry little information individually, we try to combine them together to see if the degree of polarization (DOP) (defined as Eq. (2.12)) can tell more. The comparison between the radiance image and DOP image for the same case is
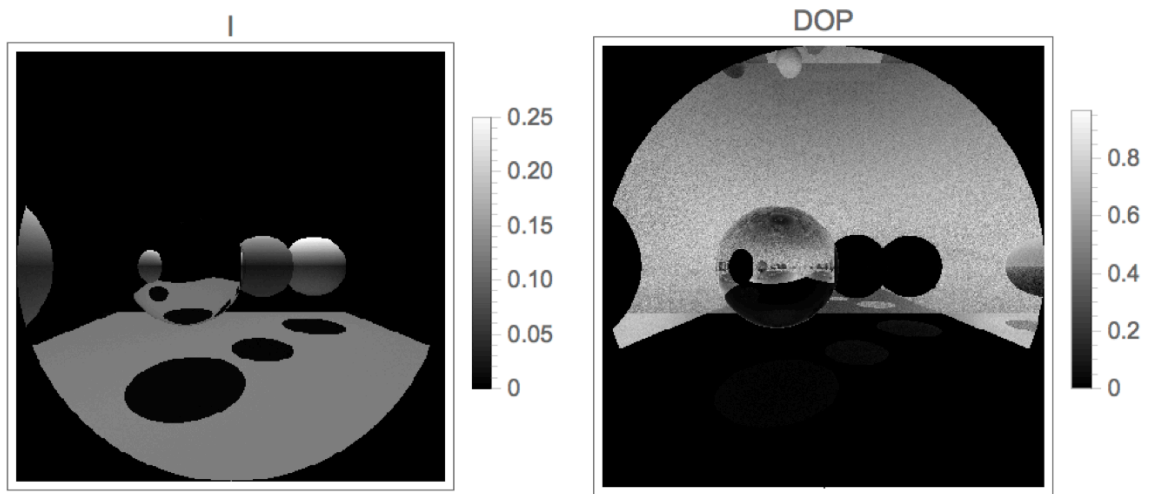
Figure 3.11: Underwater images of radiance and DOP, when the optical depth between the ocean surface and the spheres is 0.2. We assume the atmosphere layer has an optical depth of 0.15 with Rayleigh scattering (single scattering albedo 1.0), which is the characteristic of the earth's atmosphere. Inside the ocean, light scattering has HG phase function (single scattering albedo 0.85) with asymmetry factor g=0.93 and Rayleigh type reduced Mueller matrix.

shown in Figure 3.10. The DOP image can convey much better contrast compared with the three components individually. All the Lambertian surfaces display very small DOP since the reflection on Lambertian surfaces is totally unpolarized. The DOP becomes comparably high at points further away. The high DOP comes from the path radiance since scattering with a Rayleigh type reduced Mueller Matrix can produce a large DOP at 90 degree scattering.

Then what will happen when the scattering is very weak. Figure 3.11 shows the underwater images of radiance and DOP, when the optical depth between the ocean surface and the spheres is just 0.2. We have very sharp contrast for both the two images, since without too much scattering the direct beams from the targets can convey their unique scattering information. For the radiance image, the top of the mirror sphere is black, in contrast to the bright spot when the optical depth is large. This can be explained by that no photons

from the top of the mirror sphere can reach the detector after specular reflection from it. The image of DOP is really fabulous for this case. We can see clearly the mirror sphere, the surrounding glass walls as well as the air-ocean interface. We can also see clearly these beautiful surrounding images not only on the mirror sphere surface, but also on the glass walls and on the air-ocean interface. In this weak scattering case, the degree of polarization conveys much more imaging information than the radiance. Since many marine animals are capable of detecting light polarization while humans can only see radiance, maybe the world in their eyes is much more spectacular than ours. Note the difference between the image of the bottom on the glass wall and the image of the bottom on the mirror sphere. This is because the mirror reflection conserves the polarization information while the glass reflection changes the polarization dramatically.

From the two cases, we can see polarization information contains a lot of useful information about the surrounding light field. Sometimes it can even convey more information than the radiance. Thus the polarization can always be used to improve the underwater imaging quality.

3.5.3 Polarizer imaging

To learn about the real ocean water polarization information, we want to study the imaging of several polarizers which are placed vertically in the ocean. Dr Alex Gilerson's Group from City College of New York made some measurement and their measurement instrument is as shown in Figure 3.12. The polarizers and a piece of silver mirror were stuck together and they were placed vertically in water. The camera was about 1m away from the mirror and the frame to which the camera and the mirror were attached was allowed to rotate, both clockwise (as shown) and counterclockwise with computer-controlled thrusters. Measurements were taken on July 10th, 2012 in Curacao (near oil terminal). The sun azimuth angle (clockwise from North) was 81 degree, sun elevation (from horizon) was
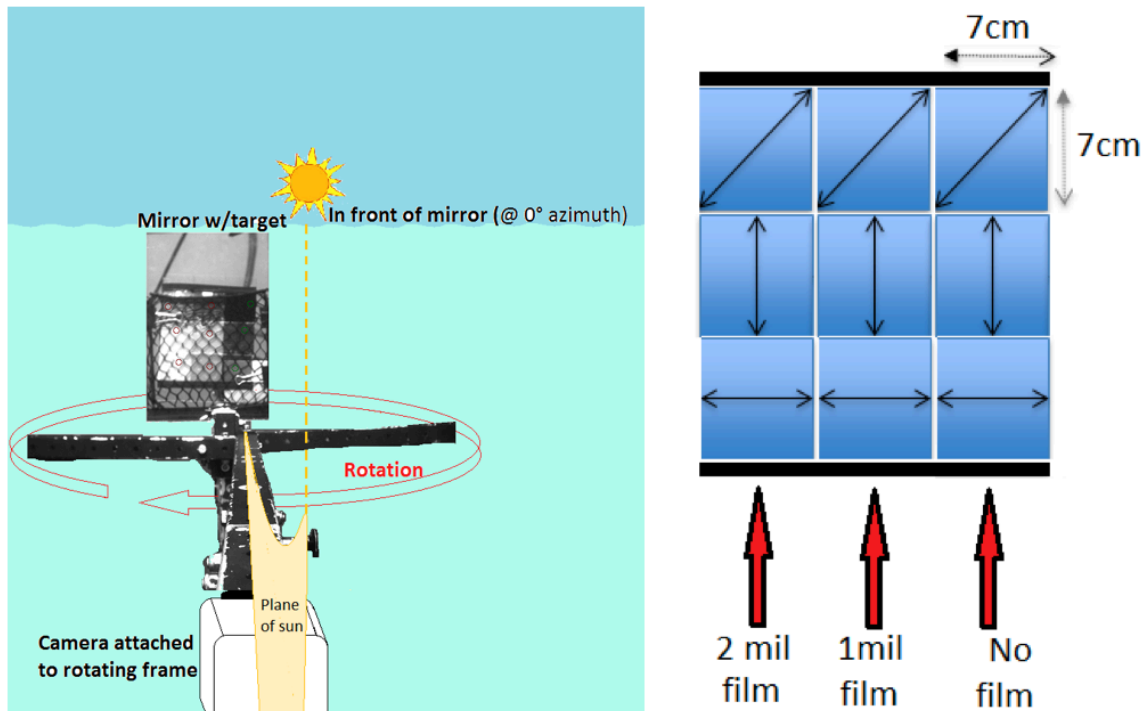
Figure 3.12: The measurement instrument for polarizer imaging by Dr Alex Gilerson's Group from City College of New York. The polarizers and a piece of silver mirror were stuck together and they were placed vertically in water and the camera was about 1m away from the mirror. The frame to which the camera and the mirror were attached was allowed to rotate, both clockwise (as shown) and counterclockwise with computer-controlled thrusters. The sun azimuth angle (clockwise from North) was 81 degree, sun elevation (from horizon) was 43 degree, the depth was 2.91 ± 0.09 meters, and wind speed was about 3m/s.

43 degree, the depth was 2.91 ± 0.09 meters, and wind speed was about 3m/s. Several simulations for the exactly same system are made using the backward Monte Carlo code. The atmosphere layer is assumed to have an optical depth of 0.15 with Rayleigh scattering (single scattering albedo 1.0). Their measured phase function is used for light scattering in the ocean and Rayleigh typed reduced Mueller matrix is assumed. The extinction coefficient is $0.16m^{-1}$ and the single scattering albedo is 0.85. The asymmetry factor g=0.925, which means the scattering is strongly dominated at forward direction.
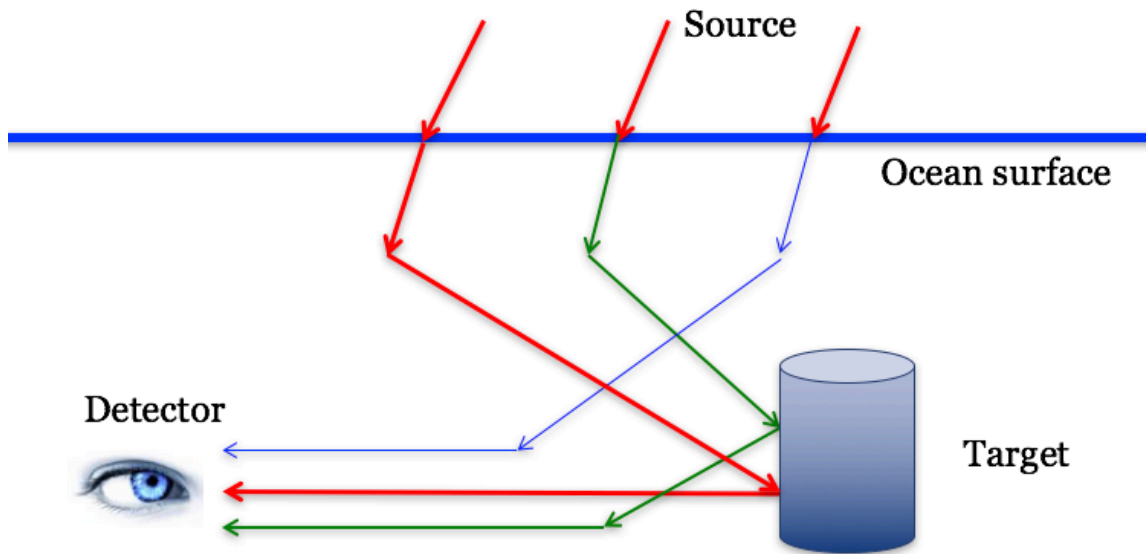
Figure 3.13: Three different types of radiance that contribute to the images: radiance directly from the target(target radiance), radiance without interaction with the target(path radiance) and radiance with scattering between the target and camera(target radiance with scattering).

One powerful feature of Monte Carlo simulation is that we can track the history of each photon arriving to the detector. There are three different types of radiance that contribute to the images, as shown in Figure 3.13: radiance directly from the target(target radiance), radiance without interaction with the target(path radiance) and radiance with scattering between the target and camera(target radiance with scattering). The target radiance can convey the information about the target, while the other two types of radiance will make target image blurred by introducing surrounding light information. Monte Carlo simulation can give us the contribution of each component to the final signal.

For example, the contributions of the three different types of radiance for the four polarizers, when the camera is 1m away from the target, are shown in Figure 3.14. The scattering by the sea water is strong enough such that the target radiance and the path radi-

47
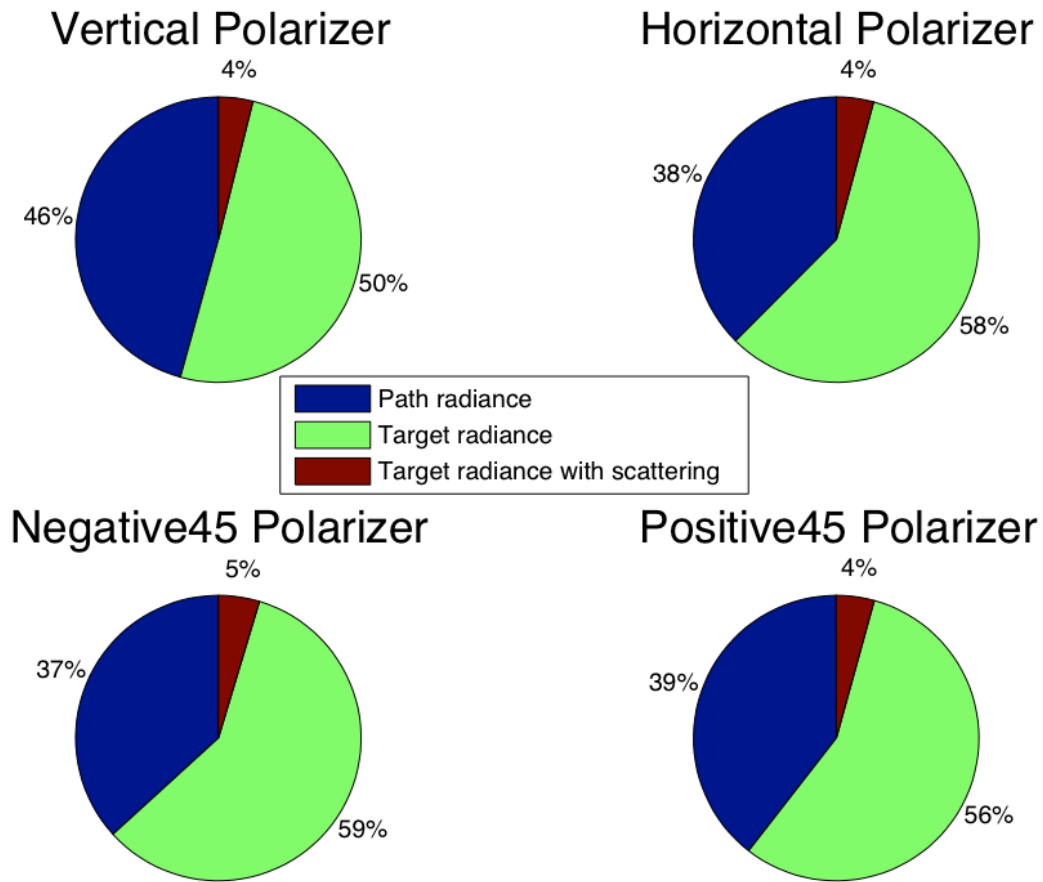
Figure 3.14: The contributions of the three different types of radiance for the four polarizers, when the camera is 1m away from the target. The extinction coefficient in the ocean is $0.16m^{-1}$ and the single scattering albedo is 0.85.

ance have nearly the same contribution even though the distance between the camera and target is only 1m. We can expect the target radiance contribution will drop very quickly as the object goes further away from the camera. The relation between the target radiance contribution and the optical depth from the target to the camera is numerically plotted in Figure 3.15. Since the ocean light is mainly horizontally polarized, the horizontal polarizer
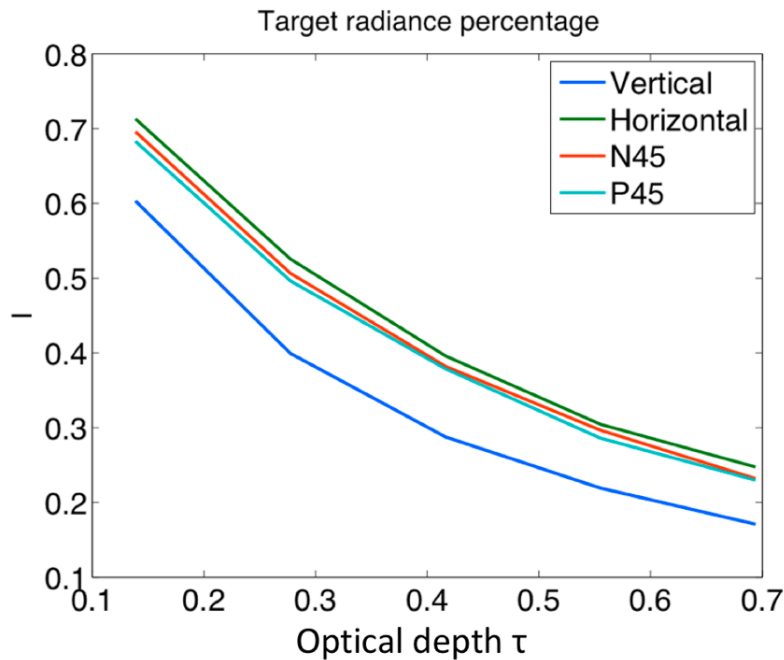
Figure 3.15: The numerical relation between the target radiance contribution and the optical depth from the target to the camera.

always has the highest target radiance contribution because horizontally polarized light is easier to be reflected back by a horizontal polarizer. While the vertical polarizer will kill horizontally polarized light, thus it always has the lowest target radiance contribution. We can expect that at a distance of 5m with extinction coefficient in the ocean $0.16m^{-1}$, the target radiance contribution will be less than 20% and the ocean imaging will be very

blurred, with an optical depth 0.8. Strong scattering and absorption kills the target radiance and the path radiance becomes dominant. This is the direct reason why underwater imaging is very challenging.

Since a polarizer is 100% polarized, the DOLPs of these polarizers will be close to 1 when the camera is close enough. As the camera goes away, the DOLPs decrease to certain values (nearly 25%), as we can see in Figure 3.16. Same thing happens for the AOLPs:
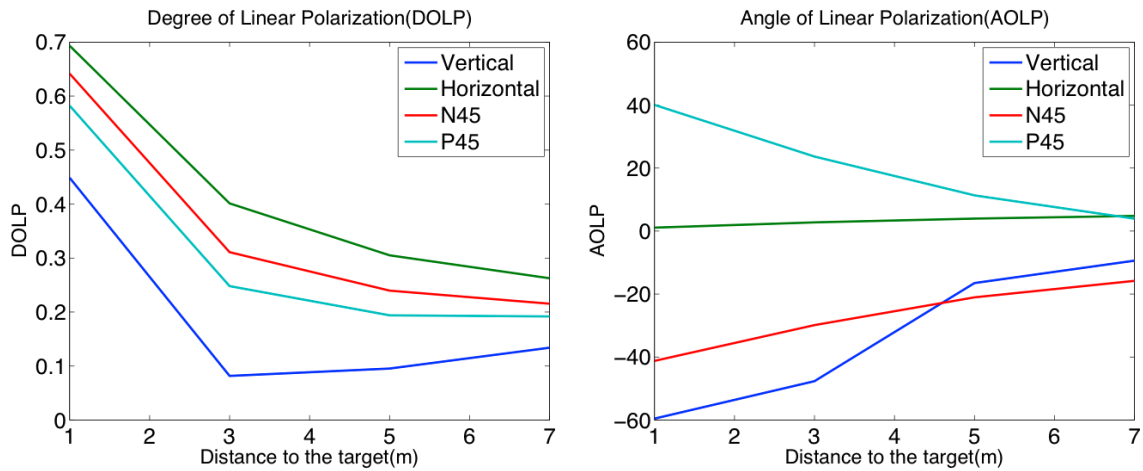
Figure 3.16: The DOLP and AOLP vs the distance between the target and the camera.

all the ALOPs decrease from their theoretical value to 0 as the distance from the target to the camera increases. This can be explained by that when far away enough, path radiance, which is mainly horizontally polarized with a DOLP about 25%, will become dominant.
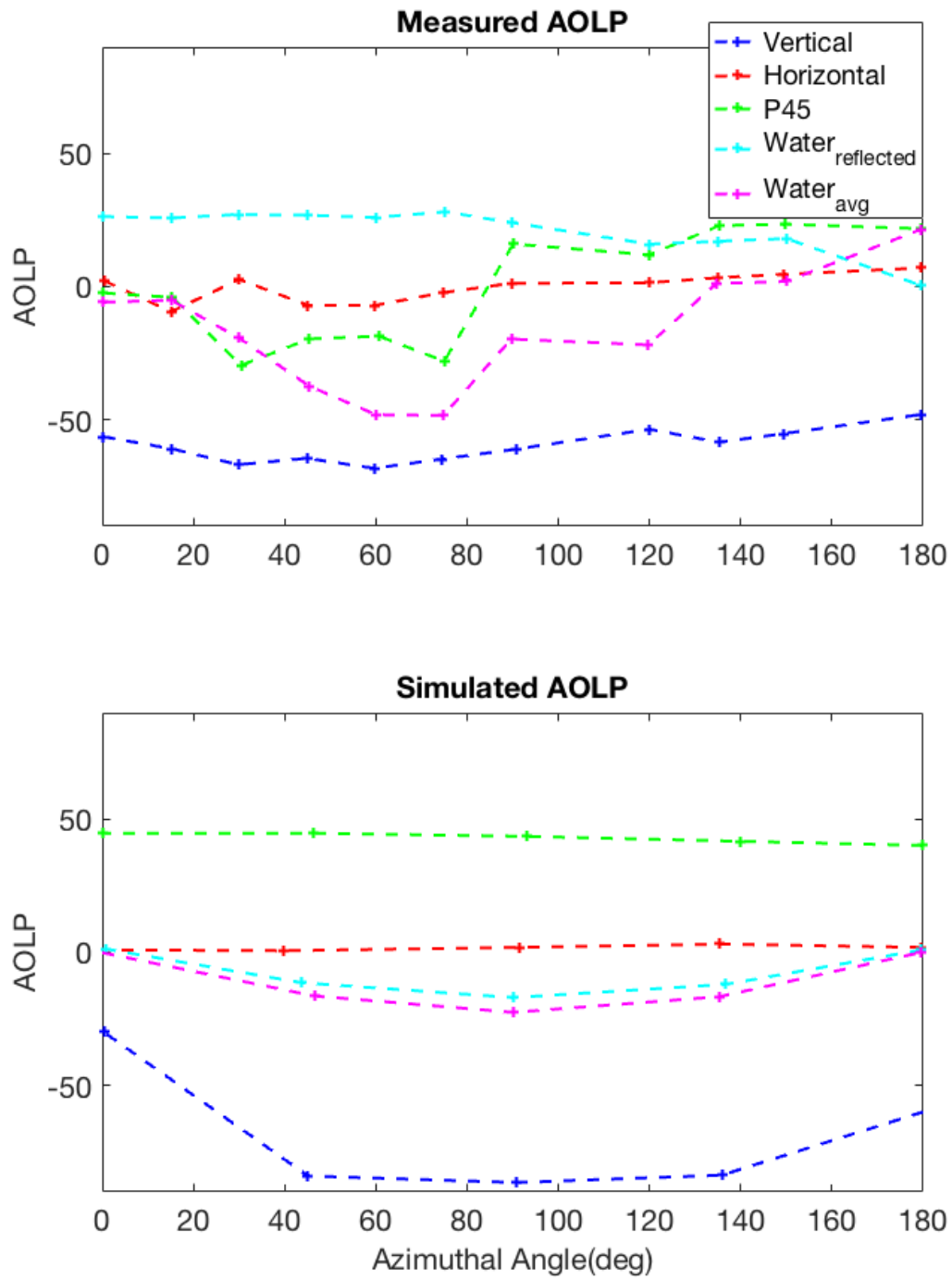
Figure 3.17: Distribution of AOLP as a function of azimuthal angle.
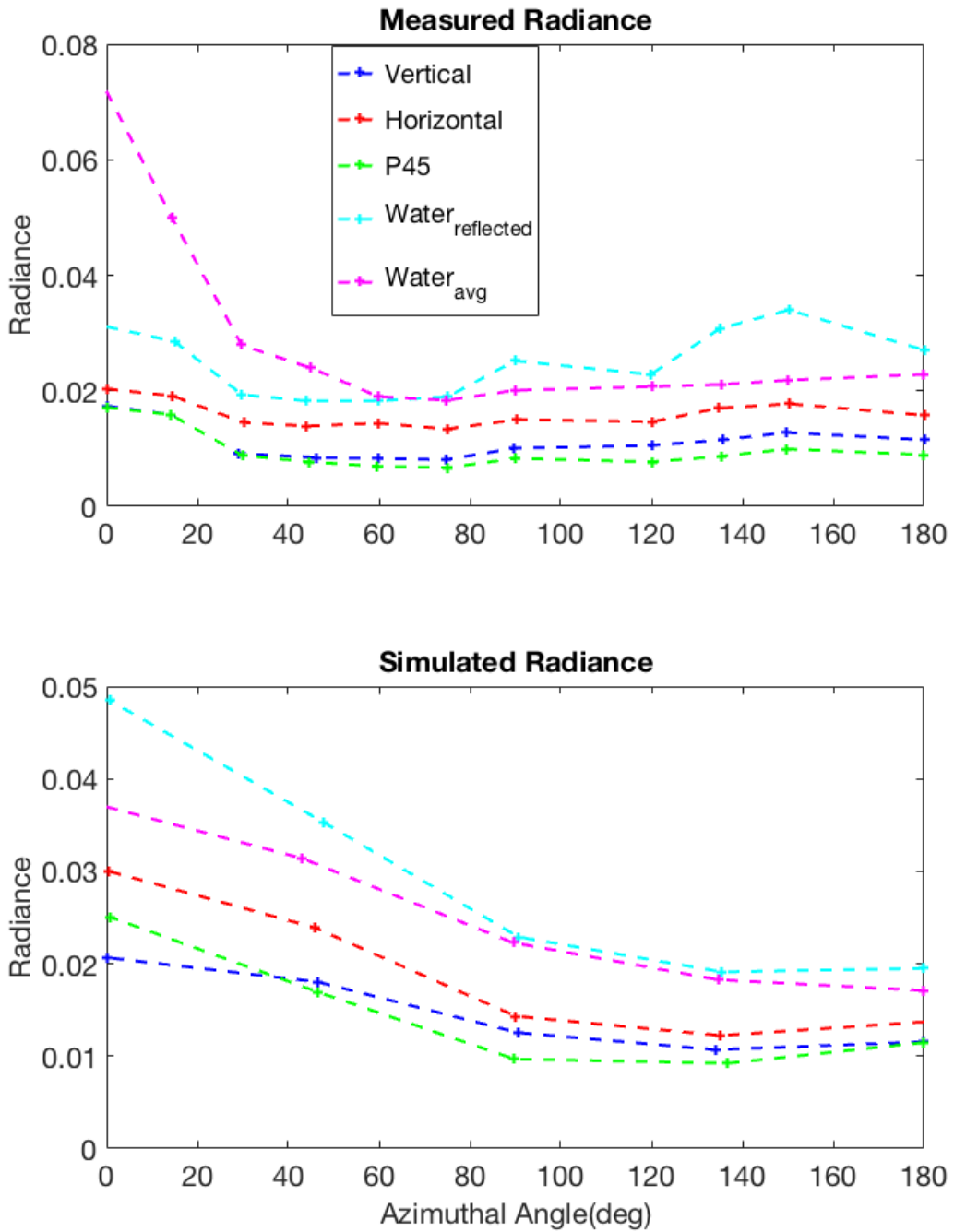
Figure 3.18: Distribution of radiance as a function of azimuthal angle. We define the 0 azimuthal angle as the sun is in front of the target.

Images of the polarizers, the mirror and water areas outside the target are simulated with different azimuthal angles from 0 to 180 deg. Here we define the 0 azimuthal angle as the sun is in front of the target. Distribution of radiance as a function of azimuthal angle is shown in the Figure 3.18. As the azimuthal angle increases, the target will be rotated away from the sun, thus the radiance will decrease. We have the same trend as the measured result, however, we couldn't get good numerical agreement.

Distribution of ALOP as a function of azimuthal angle is shown in the Figure 3.17. We have the AOLP very close to the theoretical values, however, again no good numerical agreement could be reached.

4. EFFECT OF BOTH COHERENT AND INCOHERENT BEAMS ON BOTH FORWARD AND MULTIPLE SCATTERING FOR AN ENSEMBLE OF PARTICLES

In many biological organisms, organic particles are very densely packed together, for example, the chromatosomes in a chromatophore cell and the erythrocytes in human blood. For an ensemble of particles, the photons will be scattered many times before reflected or transmitted out. Multiple scattering makes it extremely difficult to simulate the light scattering. A big forward-scattering peak, which is caused by the coherent effect, will always appear. Because the filling particles, the chromatosomes and the erythrocytes, are spherical, we can try to model the chromatophore cell or the blood system by an imaginary spherical volume enclosing many small spheres. We seek simple simulation models for the complex scattering media, by comparing exact scattering results with results with approximations.

4.1 Some numerical models

4.1.1 Phase shift of single particle at the forward direction

For particles with mirror and rotational symmetry, the exact forward wave behaves like scalar propagation and the scattering amplitude matrix reduces to identity matrix [45]. In the forward direction (denoted by 0), the complex amplitude can be expressed as

$$S(0) = |S(0)|e^{i\phi_0} \tag{4.1}$$

where ϕ_0 is the relative phase shift of the scattered wave. These parameters are dependent on the particle but independent of the polarization states of the incident light. For single particles, the scattering properties are easy to compute: Lorenz-Mie theory provides an

analytical solution of S(0) for spherical particles [32], and the DDA method can be used to obtain numerical result of S(0) for non-spherical particles. Alternatively, there exists a simple approximate method, the so-called anomalous diffraction method [45]. When the particles are large and their refractive index n (relative to the surrounding medium) is close to 1, by introducing a phase lag which depends only on the particle geometry, the forward scattering amplitude can be approximated by

$$S(0) = \frac{k^2}{2\pi} \iint (1 - e^{ik(n-1)d}) dx dy \qquad (4.2)$$

where $k = 2\pi/\lambda$ is the wavenumber, d is the distance a ray of light at (x,y) travelled within the particle assuming the ray suffers nearly no deviation along z-axis, as shown in Figure 4.1. The integral will become real when the particle size is big enough [45], thus the phase shift goes to $\pi/2$ when considering the $\pi/2$ phase shift introduced by the asymptotic form of the scattered wave in the far field as in Eq. (2.15).
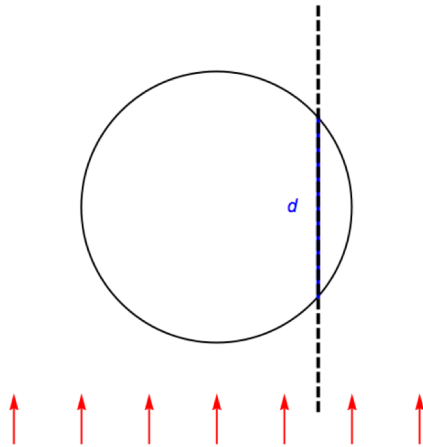
Figure 4.1: A diagram of a ray of light passing through a sphere. d is the distance the ray at a specific point travelled within the sphere assuming the ray suffers no deviation along the incident direction. The phase shift of single particle at the forward direction can be calculated using anomalous diffraction method.

4.1.2 Monte Carlo code for the spherical volume

The Monte Carlo model based on radiative transfer theory is a powerful method which can be used to solve the multiple scattering for ensembles of particles. The scattering medium is assumed statistically homogeneous in the model, which means the probability to find a scatterer at any position in the medium is the same. For such systems, the scattering variables can be obtained as following. First, the single scattering properties for the filling spheres: the single scattering albedo, the scattering phase matrix as well as the cross sections, are calculated using Lorenz-Mie theory [32]. Then the extinction coefficient can be obtained by the product of the single extinction cross section and the number density of the filling spheres. At last, the extinction coefficient can be used to sample the scattering path length and the single scattering phase matrix can be used to sample the scattering angles. A Monte Carlo code has been developed to simulate light scattering for the spherical volume.

4.1.3 Effective medium theory

A temptingly simple method for an ensemble of particles is to approximate the composite medium as a homogenous medium with an effective refractive index. This method is called effective medium theory (EMT) [44], which is based on average Maxwell fields weighted by volume fraction at the macroscopic level. The effective refractive index of the inhomogeneous medium is determined by the volume fractions, the shapes as well as the refractive indexes of its constituents. Perhaps the Maxwell Garnett theory [44] is the most popularly used one. When only one kind of spherical particles are included in the matrix medium, the Maxwell Garnett formula can be written as:

$$\varepsilon_{eff} = \varepsilon_m \frac{2\varepsilon_m + \varepsilon + 2f(\varepsilon - \varepsilon_m)}{2\varepsilon_m + \varepsilon + f(\varepsilon_m - \varepsilon)} \tag{4.3}$$

where ε_{eff} is the effective dielectric constant of the medium, ε is the one of the inclusions and ε_m is the one of the matrix; f is the volume fraction of the inclusions. In this way, we can get the effective refractive index for the imaginary homogeneous spherical volume and simply use the Lorentz-Mie theory to calculate the scattering matrix. This is a rough but very simple model and we will use it to compare results with analytic results.

4.1.4 Partially coherent beam

We consider the partially coherent beams generated by the the Gaussian Schell-model [41], the cross-spectral density function with a coherence length σ_μ for two position vector $\vec{r_1}$ and $\vec{r_2}$ can be written as:

$$W(\vec{r_1}, \vec{r_2}) = A \exp(-\frac{\vec{r_1}^2 + \vec{r_2}^2}{4\sigma_s^2}) \exp(-\frac{\vec{r_1}^2 - \vec{r_2}^2}{4\sigma_\mu^2}) \qquad (4.4)$$

where σ_s is the width of the beam and A is a constant independent of the positions. We can represent the partially coherent beam with an ensemble of random fields using the angular spectrum representation [51]. We use the code in [51], which is modified from the original DDA code. The width of the beam σ_s is taken to be infinity and the influence of the coherent length σ_μ of the incident beams on the scattering matrix is studied for both single sphere and an ensemble of spheres.

4.2 Numerical results and discussion

4.2.1 Phase shift for single particle

First we applied the anomalous diffraction method to calculate the phase shifts for single particles with various sizes and various shapes. The incident wavelength is 0.435um in the ambient medium, whose refractive index is 1.33. The results are shown in Figure 4.2. To validate this method, we compared the approximate results with the accurate results, i.e. phase shift results from Mie theory for spherical particles and phase shift results from the
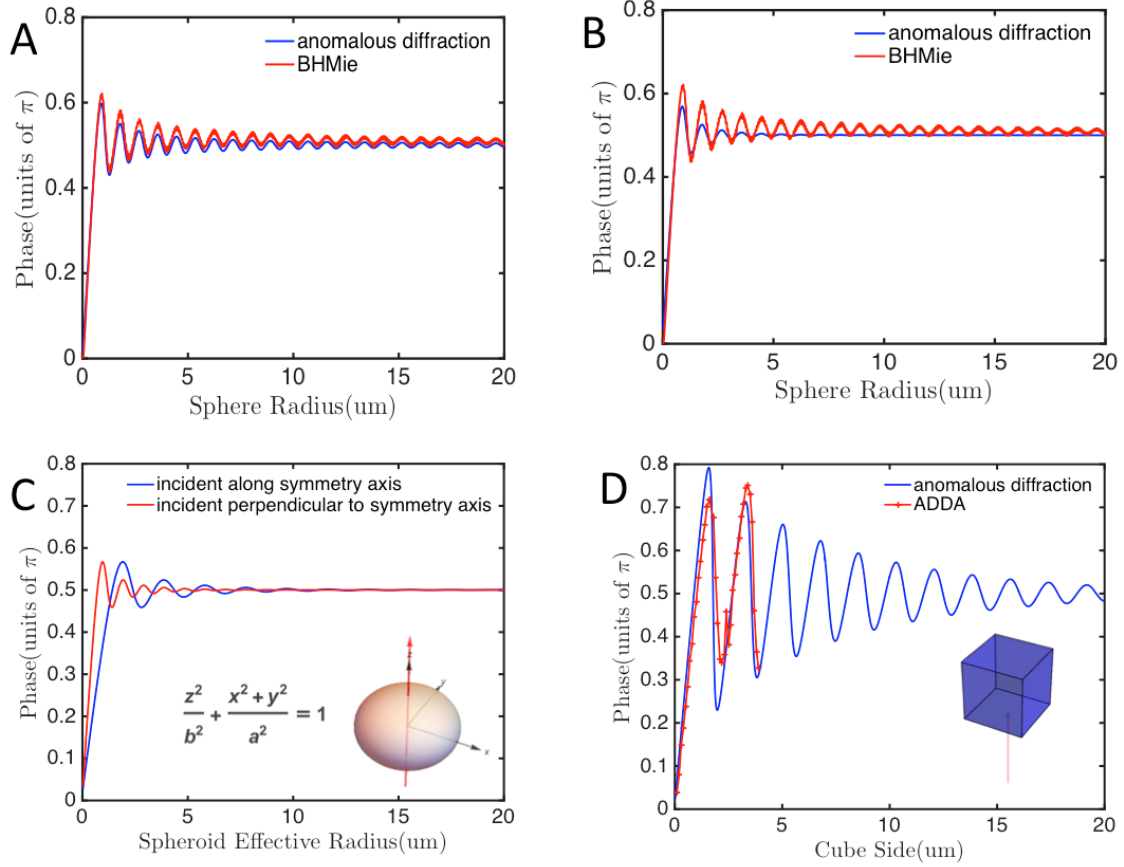
Figure 4.2: Phase shifts for single particles versus effective radius. The incident wavelength is λ=0.435um. (A) Comparison of results computed by the anomalous diffraction method and Lorenz-Mie theory for a sphere with refractive index n=1.244. (B) Same as (A) except that refractive index n=1.244+i0.013. (C) Phase shifts for two different incident directions of an oblate spheroid (a/b=2) with refractive index=1.244+i0.013 using the anomalous diffraction method. (D) Same as (A) but the results are for a cube with refractive index=1.244+i0.013 for face on incidence.

ADDA for cubic particles, as shown in panels A, B and D of Figure 4.2. Even though the anomalous diffraction method is valid only when the particles are large and their refractive index is close to the surrounding medium, we obtained good agreements for different-sized particles with relative refractive indices larger than unity. Thus the simple anomalous diffraction method can be used as a good approximation of S(0). The relative phase shift is roughly in the range $[0, \pi/2]$, which means even for different-sized scatterers, the forward scattered waves are quite coherent. Especially, when the particle size deviation is small or when all the particles are quite large, the phase shifts of the particles will be very close to each other. This means the forward waves will be completely coherent: thus an ensemble of N particles will produce a scattered amplitude of N times that for a single particle while the scattered radiance will increase by N^2, if the particles are sparsely packed and all the particles can be illuminated by the incident beam. As shown in panel C of Figure 4.2, the phase shifts with different incident directions will not be the same for non-spherical particles because of the phase lag difference along different light paths. However, the difference is again quite small and the scattered waves will behave quite coherently. In addition, we can see that from panel B of Figure 4.2, with a complex refractive index, the relative phase goes to $\pi/2$ more quickly with increased sizes due to absorption. Thus we can expect more coherent effects with stronger absorption.

4.2.2 Coherent forward scattering and multiple scattering

Since the phase shift deviation for single particles is small, the effects of the filling particles on the forward scattering were investigated for an ensemble of particles. We put 100 small particles with random positions into an imaginary spherical volume with radius R=2um. The incident wavelength is 0.435um and all the small particles have the same refractive index n=1.244+0.013i. Numerically exact methods, MSTM for spheres and ADDA for non-spherical particles, are used to calculate the Mueller Matrix components
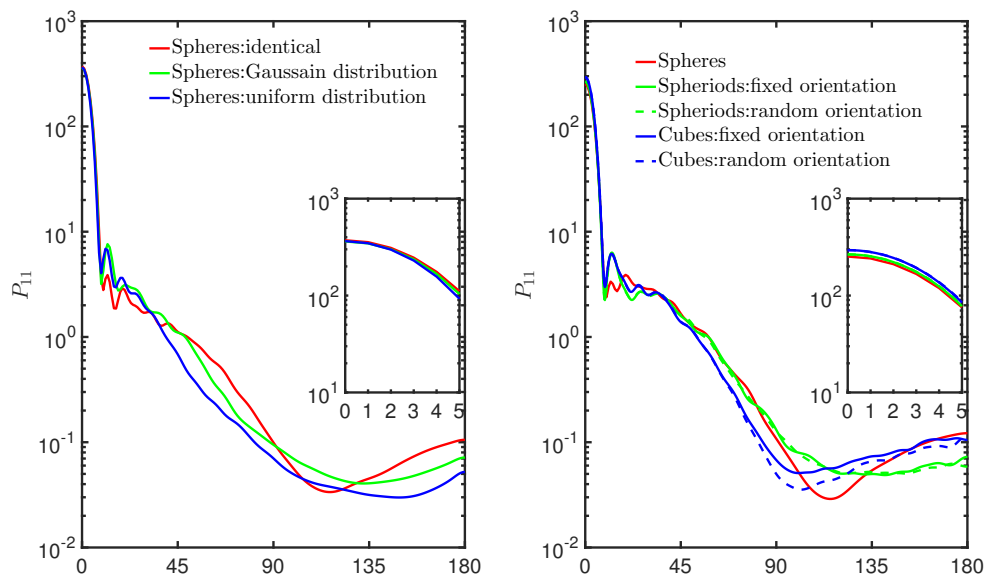
Figure 4.3: Mueller Matrix components for 100 spheres in a spherical volume with radius R=2um, incident wavelength λ=0.435um, refractive index n=1.244+i0.013 and volume fraction 0.057. In the left figure, identical size means all the spheres have the same radius 0.166um; the Gaussian size distribution has an average radius 0.166um and standard deviation 0.07um; the uniform distribution over the interval [0.096, 0.236] also has an average radius 0.166um. In the right figure, the filling particles are all the same in size for each case. They all have an effective radius r=0.166um (the effective radius is defined as the radius of an equivalent sphere with the same volume as the particle), but they have different shapes and orientations.

of the system. The results are shown in Figure 4.3. In the left figure, the filling particles are all spheres with same average radius r=0.166um, but they have different size distributions. In the first case, the spheres have the same size; in the second case, the spheres have a Gaussian size distribution; in the third case, the spheres are uniformly distributed. We define the effective radius or the effective size of a particle as the radius of an equivalent sphere with the same volume as the particle. In the right figure, the filling particles are all the same in effective radius (r=0.166um) but they have different shapes and orientations. We can see that for the 7 different cases, the ensembles of particles have the same forward phase function peak, regardless of the size distribution, the shape as well as the orientation of the filling particles. This can be explained by the fact that the forward scattered waves of individual particles are completely coherent and they will add together coherently. Thus the forward scattering of an ensemble of particles is dominated by the coherent effect, the intensity distribution of which depends on the effective size but is independent of the internal particle composition.

In the chromatophore cell, the surrounding muscle fibers can change the chromatosome density by manipulating the cell to expand or contract. We simulate the density changing by putting different number of chromatosomes into a fixed-sized spherical volume. Again the incident wavelength is 0.435um and all the chromatosomes have the same refractive index n=1.244+0.013i. The results are shown in Figure 4.4A. When the number of chromatosomes N is smaller than 200, which means the volume fraction is smaller than 10%, both the forward amplitude S(0) and the scattering cross section σ will change linearly with N. In this case, the chromatosomes are far apart from each other and the scatterings are approximately independent. A volume fraction of 10% means the average particle distance is about twice the particle diameter; this agrees with the criterion for independent scattering in [14]. However, as N increases and the particles are close to each other (volume fraction larger than 20%), both S(0) and σ are no longer linearly propor-
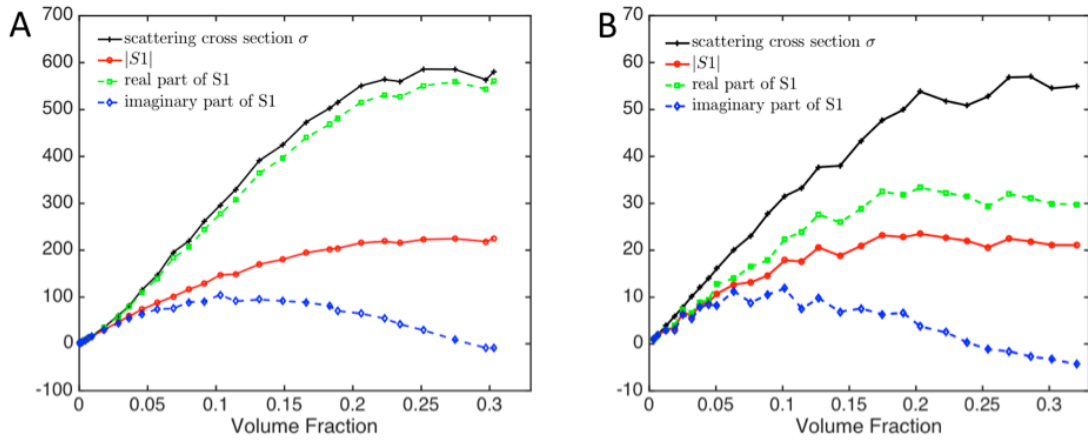
Figure 4.4: Forward amplitude values versus the volume fraction. All the values are normalized by the value for a single sphere. (A) Chromatophore cell, simulated by a spherical volume (R=2um) filled with chromatosomes (r=0.166um): λ=0.435 um, n=1.244+i0.013. (B) Blood system, simulated by a spherical volume (R=18um) filled with spherical erythrocytes (r=2.646um): λ=0.376 um, n=1.0226+i0.001.

tional to N, instead they will approach some upper bound. This can be interpreted as a multiple-scattering effect: particles occult other particles along the beam path by attenuating the incident light. Similar results for the blood system are shown in Figure 4.4B. At quite different size scales, the same conclusions can be drawn here. As the number of erythrocytes N becomes larger than 40, multiple scattering begins to have an impact. In total, an ensemble of N particles will produce a scattered radiance of N^2 times that for a single particle when the volume fraction is smaller than 10%, however, the scattered radiance will reach a plateau as a result of multiple-scattering when the particles are closely packed.

Specifically, Mueller matrix components for chormatophore cells with four different filling densities were calculated to study both the forward scattering and the multiple scattering effects. The results are compared with results both from the RT model and from the EMT method, as shown in Figure 4.5, Figure 4.6, Figure 4.7 and Figure 4.8. In Fig-

ure 4.5 and Figure 4.6, when the chromatosomes are packed sparsely, the reduced Mueller matrix elements for the Monte Carlo and the MSTM are exactly the same, and the phase functions agree very well except for a forward coherent peak (angle width about 10°) in the MSTM result. Note that light beams used in the RT model are treated as non-coherent since the phase of each scattering is ignored, while in MSTM all coherence effects are accounted for. The forward scattering peak, which causes the only difference, is just a coherent effect caused by strong constructive interference. This tells us that the independent scattering approximation is valid and the Monte Carlo method is a feasible, simple simulation method when the volume fraction is small. However, as volume fraction increases (larger than 10%, as shown in Figure 4.7 and Figure 4.8), the angle widths of the forward coherent peaks will increase (to about 20°) and a deviation between the two results begins to appear. This is because multiple scattering becomes important and it changes the features of the Mueller matrix components. Especially, we can see that P_{22}/P_{11} deviates further from unity as the volume fraction increases. An interesting result is that the EMT method and the MSTM method give the same forward scattering patterns. This again can be explained by the fact that the scattering is dominated by the diffraction pattern near the forward direction, the intensity distribution of which depends primarily on the effective size but is independent of the particle configurations.

Multiple scattering by particles in the volume makes the scattering properties deviate from single scattering. But what is the limit and when will the volume behave like a single homogeneous particle? We kept the filling volume fraction of the spherical volume the same but changed the size of the filling spheres. The Mueller matrix components for different cases are compared in Figure 4.9). We have the same forward pattern since all cases share the same effective size. Note those sharp oscillation peaks in the phase function pattern in the EMT Lorenz-Mie result is the unique feature of sphere scattering, which are caused by interference of the beams travelling inside the sphere since the sphere has the

63
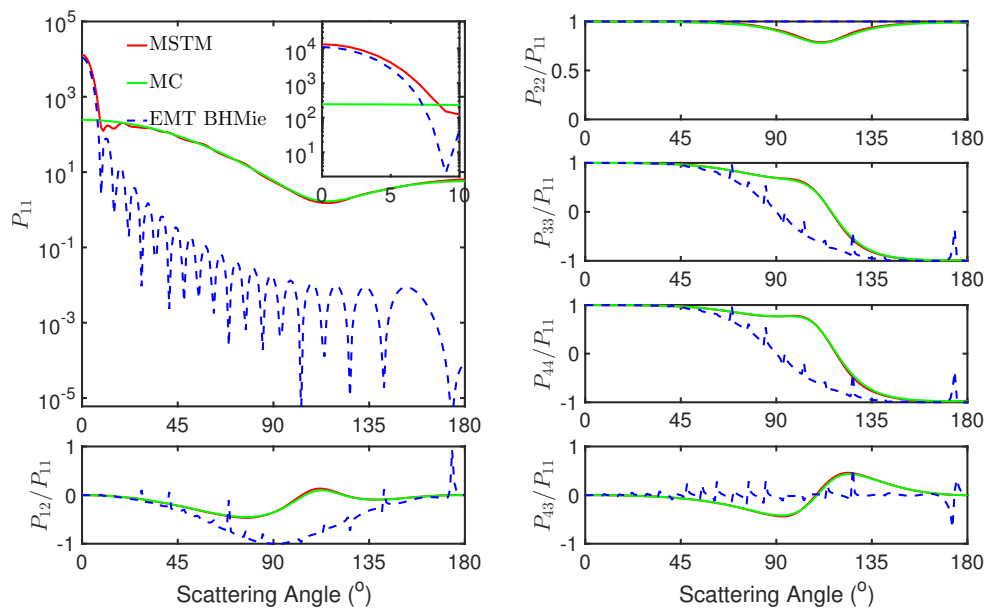
Figure 4.5: Comparison between Mueller matrix components of 50 small spheres (r=0.166um) in an imaginary spherical volume (R=2um), calculated by MSTM method and Monte Carlo method. λ=0.435 um, n=1.244+i0.013. Volume fraction=2.8%, optical depth along a diameter τ=0.1754.

Figure 4.6: Comparison between Mueller matrix components of 100 small spheres (r=0.166um) in an imaginary spherical volume (R=2um), calculated by MSTM method and Monte Carlo method. λ=0.435 um, n=1.244+i0.013. Volume fraction=5.7%, optical depth along a diameter τ=0.3508.

Figure 4.7: Comparison between Mueller matrix components of 200 small spheres (r=0.166um) in an imaginary spherical volume (R=2um), calculated by MSTM method and Monte Carlo method. λ=0.435 um, n=1.244+i0.013. Volume fraction=11.4%, optical depth along a diameter τ=0.7016.

Figure 4.8: Comparison between Mueller matrix components of 400 small spheres (r=0.166um) in an imaginary spherical volume (R=2um), calculated by MSTM method and Monte Carlo method. λ=0.435 um, n=1.244+i0.013. Volume fraction=22.8%, optical depth along a diameter τ=1.4033.

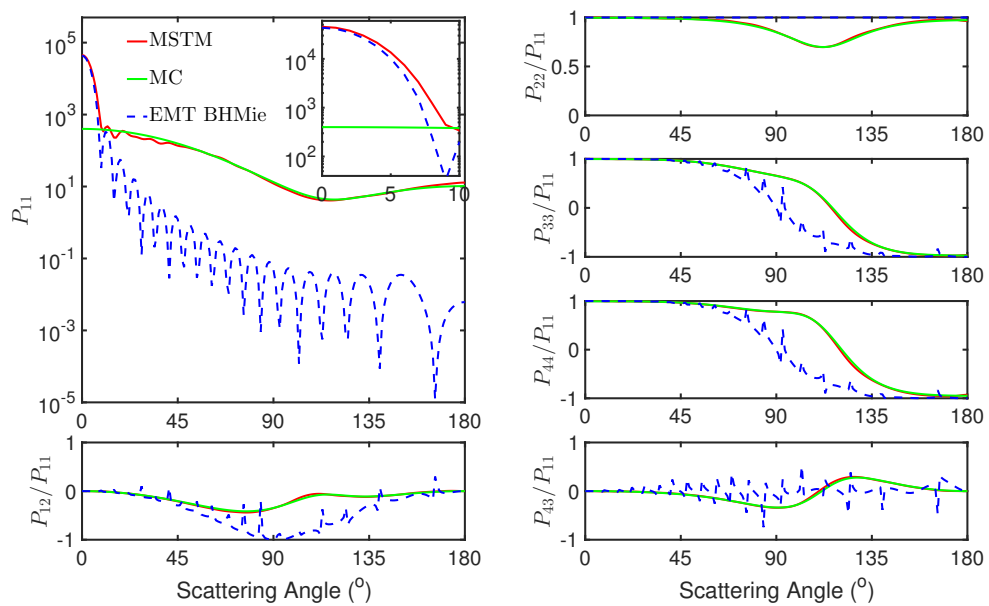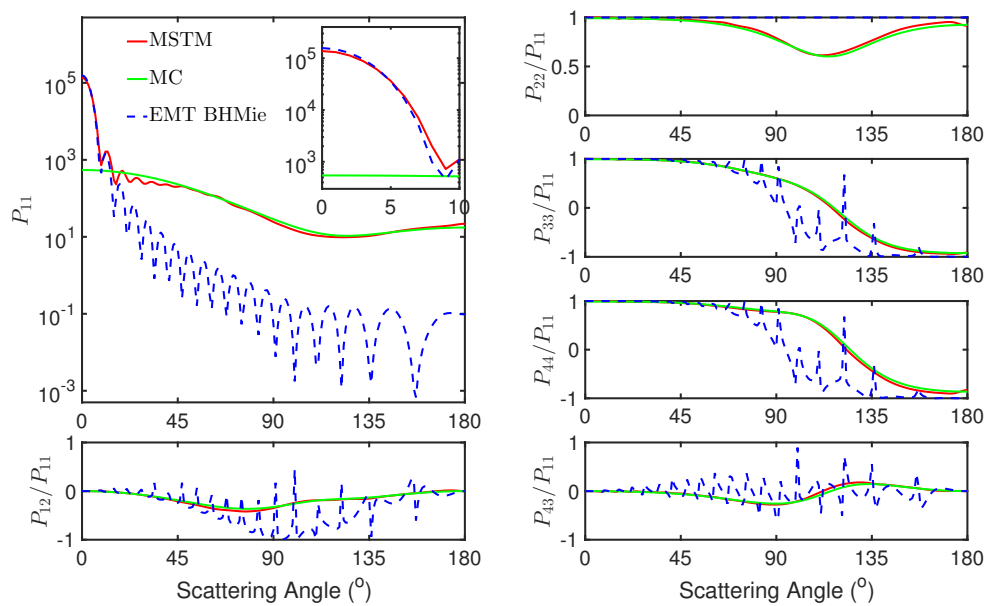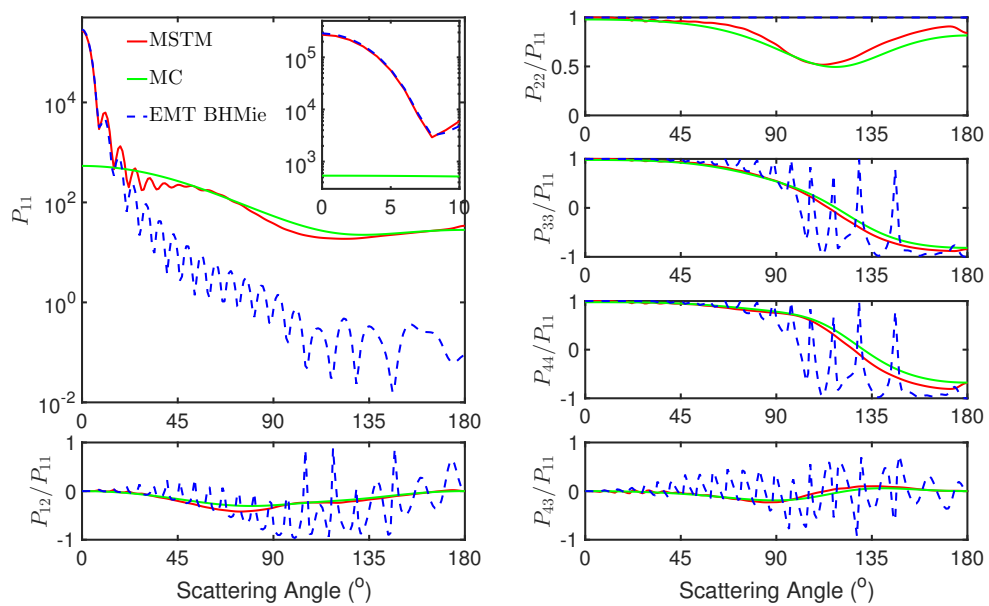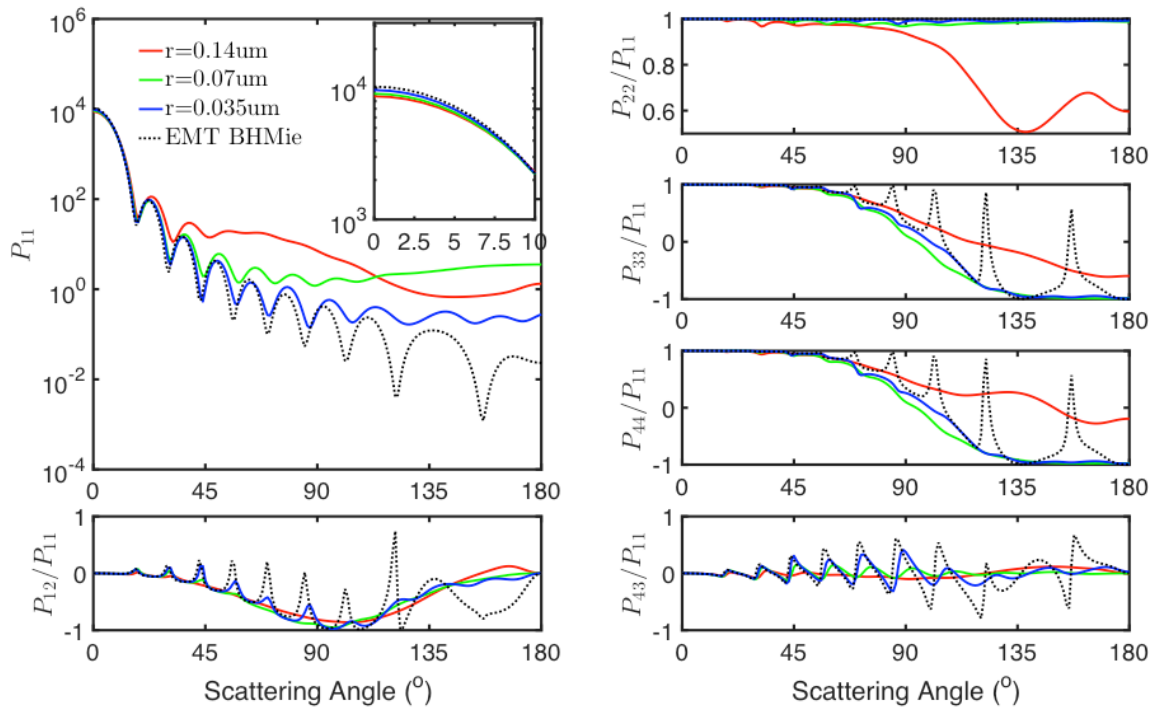Figure 4.9: Comparison between Mueller matrix components of a spherical volume (R=2um) filled with different-sized small spheres: the volume fraction is fixed at 22.8%, λ=0.435 um and n=1.244+i0.013.

highest level of symmetry. When the filling particles are large, the spherical volume isn't a continuum but instead it consists of a collection of discrete spheres, and therefore we shouldn't expect to see these sharp resonances which occur for a homogeneous sphere. However, as the filling spheres become smaller, it will become harder for the incident light to distinguish these discrete particles. With the radius of the small spheres r=0.035um as shown in the blue curve in Figure 4.9), the Muller matrix components display the same oscillations peaks. We can expect the spherical volume will behave more like a single homogeneous particle with even smaller filling spheres, just like a sphere composed of dipoles in the ADDA method. Unfortunately, organic particles in human or animal tissues typically have a size much larger than 0.035um, therefore, we couldn't use the simple EMT method to simulate the multiple scattering of the composite media.

4.2.3 Partially coherent beam

As the forward scattering patterns are mainly caused by the constructive interference which originates from the complete coherence of the forward scattered beam, it is instructive to study what will happen when partially coherent beams are incident. There are two important characteristic lengths compared with the coherence length of the incident light for a volume of particles: the size of single particle and the size of the volume. Thus the Mueller matrix components were calculated for both a single sphere and an ensemble of spheres with partially coherent incident beams of different coherence lengths.

We will study this for a single sphere for an incident wave of λ=0.435um, and refractive index n=1.244+i0.013, and we will consider two different cases: a sphere with radius much smaller than the wavelength (r=0.166um, similar to the chromatosome) and a sphere with radius much larger than the wavelength (r=2.17um, similar to the erythrocyte). For the first case, as shown in Figure 4.10, we can see the coherence length plays an important role in determining the scattering patterns. With a large coherence length σ_μ=4λ ,

Figure 4.10: Comparison between Mueller matrix components of single small sphere (r=0.166um) calculated by the DDA method with partially coherent incident beams of different coherence lengths. λ=0.435 um, n=1.244+i0.013.
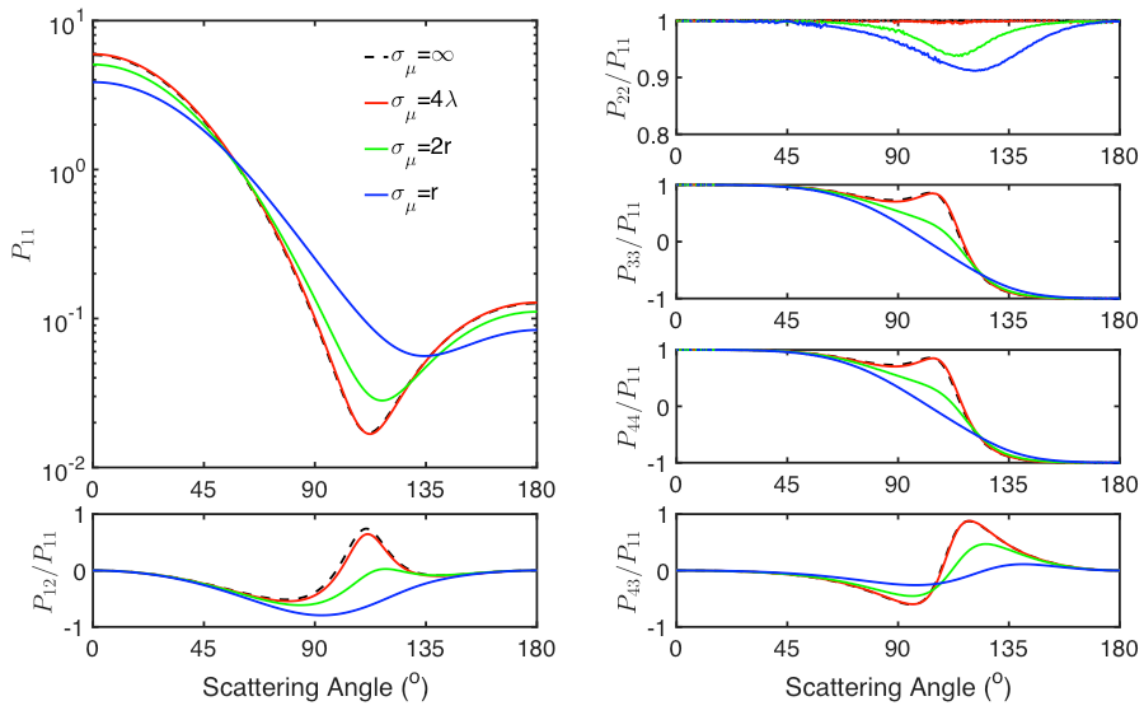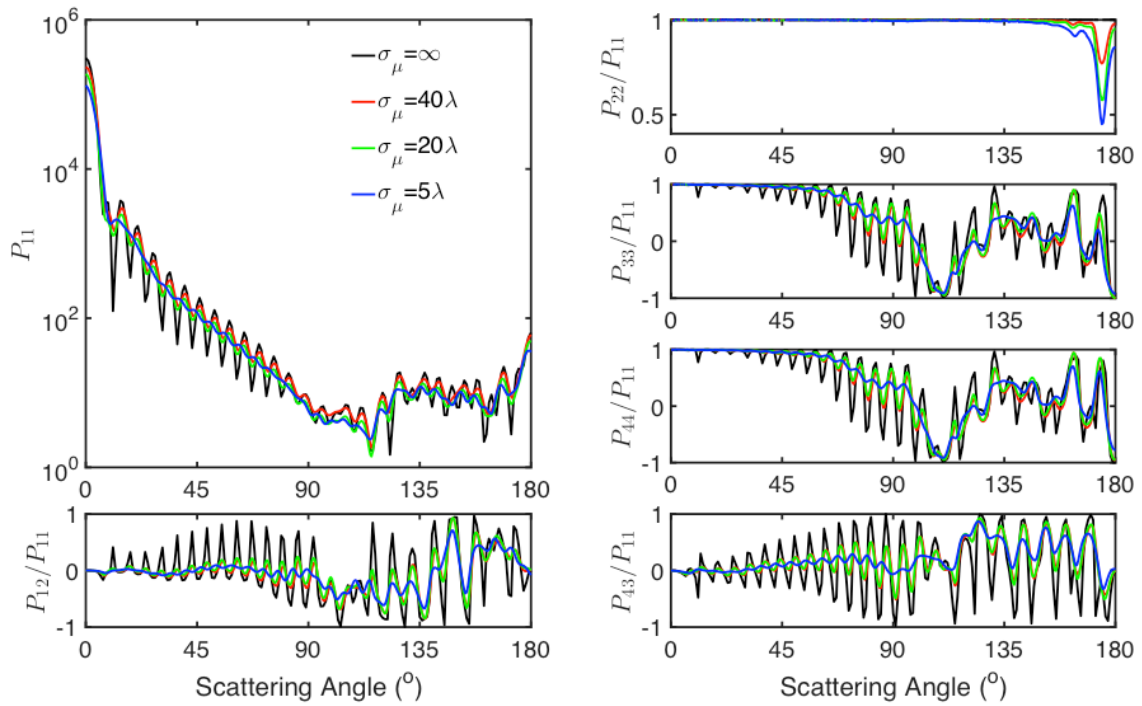
Figure 4.11: Comparison between Mueller matrix components of a single large sphere (r=2.17um=5λ) calculated by the DDA method with partially coherent incident beams of different coherence lengths. λ=0.435 um, n=1.244+i0.013.

the results approach the coherent case. As the incident field becomes less coherent, the Mueller Matrix components become smoother and more isotropic and start to lose their features. When σ_μ=r, both the forward and backward peaks in the phase function vanish and other Mueller Matrix components deviate significantly from the coherent case. However, for the case where the sphere is much larger than the incident wavelength, as shown in Figure 4.11, the influence of coherence length is dramatically different. As the coherence of the incident light deteriorates, the overall curves for Mueller Matrix components are almost the same except that the forward and backward phase function peaks become smaller and the oscillation peaks are smoothed out. Since all the peaks are consequences of coherent interference, it?s reasonable to expect this behavior when coherence is lost. In the atmosphere, many water droplets and ice crystals have an effective radius over 100um, which is larger than 60um, the coherence length of the sunlight. The scattering peaks will be weakened comparing with the coherent case. However, considering the large coherence length of the sunlight, the overall scattering pattern will be the same. As calculated by Jianping [51], we can still expect the rainbows and glories for spherical raindrops, and the halos for hexagonal ice crystals.

For a volume of small spheres, we again used the chromatophore cell as an example. A chromatophore cell (R=2um) is filled with 50 chromatosomes (r=0.166um), the incident wavelength is λ=0.435um, the refractive index is n=1.244+i0.013, and the volume fraction is about 3%. The results are shown in Figure 4.12. The P_{11} forward peak values will decrease dramatically with decreased σ_μ due to lack of coherence in the incident beam. Also as σ_μ decreases, other Mueller Matrix components features will be smoothed out, as a consequence of Rayleigh single scattering by the chromatosome. Therefore, the coherence length impacts the scattering patterns a great deal for an ensemble of small spheres when the coherence length is comparable with the size of the filling particles. Thus we must be very careful when we make measurements or simulations for this kind of system
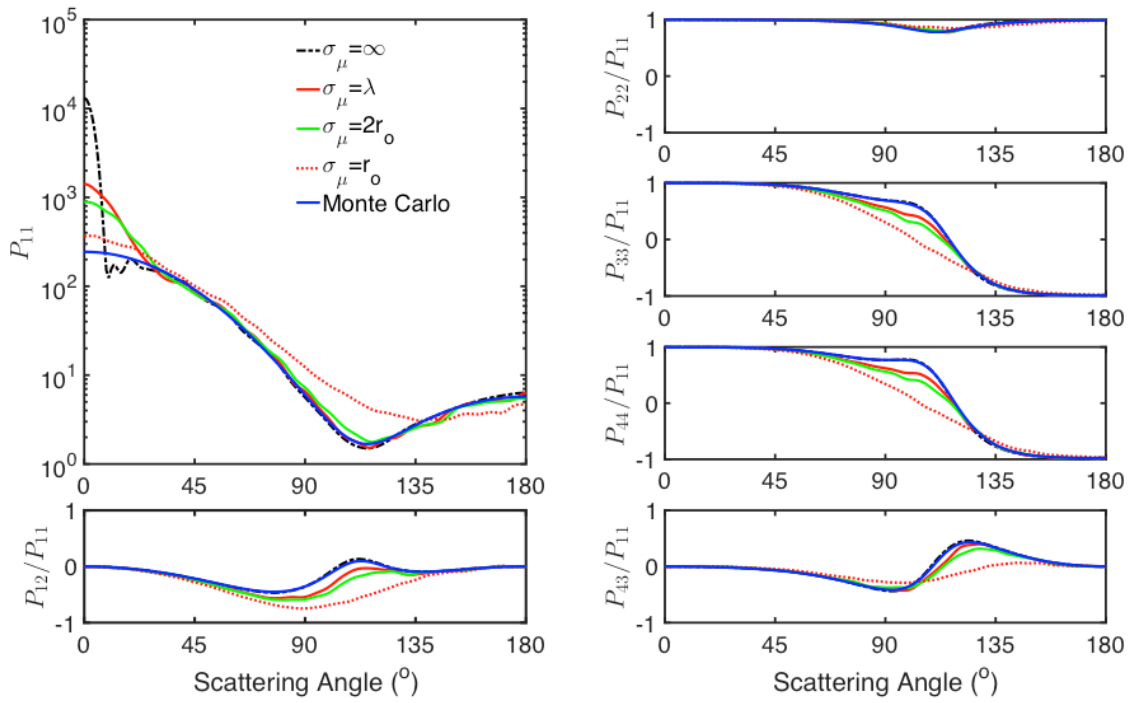
Figure 4.12: Comparison between Mueller matrix components of a chromatophore cell (R=2um) filled with 50 chromatosomes (r=0.166um, volume fraction=0.028), calculated by DDA method with partially coherent incident beams of different coherence lengths and Monte Carlo method. λ=0.435 um, n=1.244+i0.013.
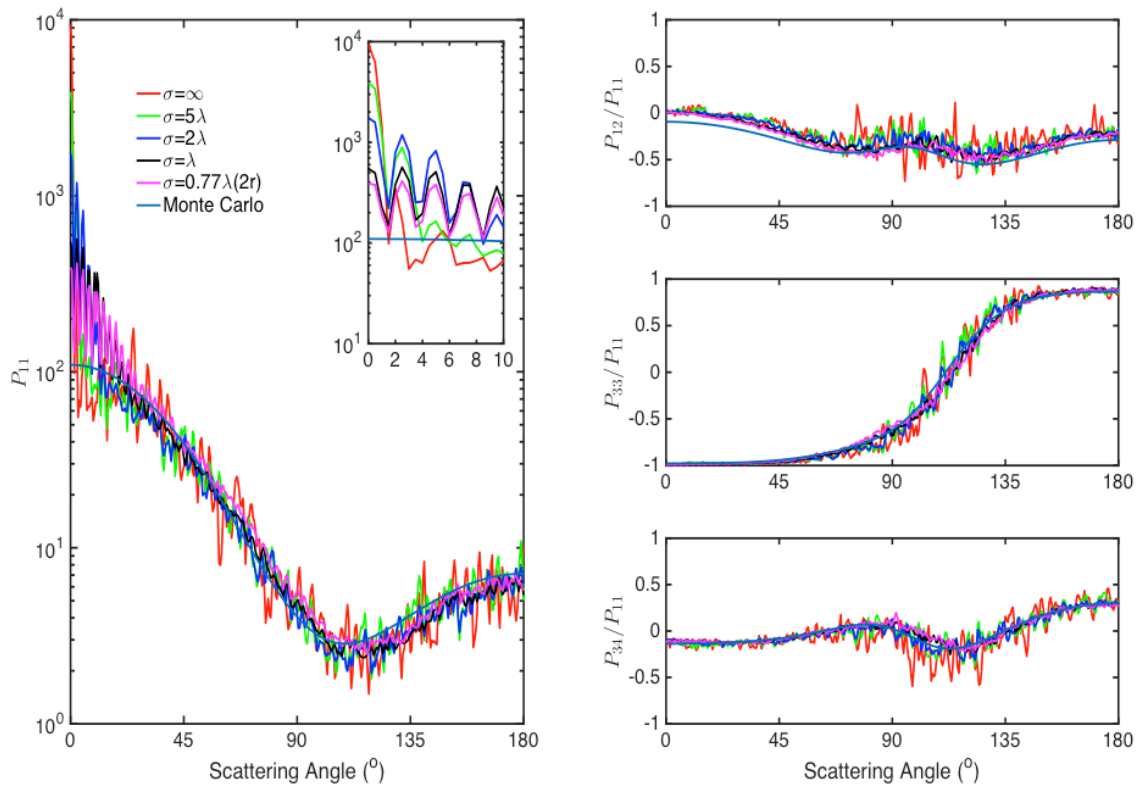
Figure 4.13: Comparison between Mueller matrix components with partially coherent incident beams of different coherence lengths, for a circular area (R=20um) filled with 100 disks (r=0.166um, the area fraction is 0.01). λ=0.435 um, n=1.244+ i0.013.

considering partially coherent beam incidence. In reality, the sizes of the scattering media are always very large, at least much larger than both the incident wavelength and the size of the included particles. To account for this, we need to increase the media volume size to better simulate the actual situation. We next wanted to expand the size of the spherical volume. Due to the speed limitation of the DDA code, we tried the simpler two-dimensional case and considered a circular area (R=20um) filled with 100 disks (r=0.166um). The area fraction is about 1% and everything else is the same as before. The results are shown in Figure 4.13. Except for the dramatically decreased forward peak as a result of decreased coherence, the reduced effective Mueller matrix components as well as the phase function, agree perfectly with the Monte Carlo results. This can be explained by the fact that only scattered waves by particles in the coherent volume will interact coherently and the sparseness of the filling particles makes the interaction similar as incoherent multiple scattering in the RT model. Given that the overall patterns for single large spheres are almost the same for different coherence lengths and multiple scattering once again washes out the single scattering features, we can expect the result for a large ensemble of large particles will agree with the RT result. Thus, with low volume fraction and large size of the filling particles, the Monte Carlo results match the DDA results when incident with a partially coherent beam. Actually, the scattering of aerosols in the atmosphere and hydrosols in the ocean is just such a case. They are distributed so sparsely in the atmosphere with large sizes compared with the sunlight. This is the reason why RT model virtually always works well for atmospheric and oceanic simulations. In addition, we can still observe the similar forward phase function diffraction patterns, only with different amplitudes for different coherence lengths.

4.3 Conclusion

The relative phase shifts of forward amplitude for single particles range in $[0, \pi/2]$ and thus the scattered waves in the forward direction always have some degree of coherence. Especially, if the particles sizes are close to each other, the relative phase shifts will be almost the same and the forward coherent peak values of the ensemble are dependent on the effective sizes of included particles but independent of their shapes, size distributions and orientations. For an ensemble of particles, the forward amplitude S(0) changes linearly with small number of the scatterers, but it will saturate as a result of multiple scattering effect when more scatterers are in the ensemble; independent scattering is valid when volume fraction is small, while multiple scattering will make the scattering deviate more from the single scattering as volume fraction become larger. The EMT theory fails to get the scattering patterns since the organic particles aren't small enough to make the scattering medium a continuum. The forward phase function peak is an effect of coherent interference and of course with decreased coherent lengths of the incident wave, the peak will decrease sharply as a result of incoherence. For an ensemble of big particles of low filling volume fraction with partially coherent beam incidence, the Monte Carlo method (or RT model) can give matched results with analytical results since the forward coherent peak vanishes and scattering events are independent. While additional attention should be paid when dealing with a volume of small particles since the increased incoherence will smooth out most scattering patterns.

5. CONCLUSIONS

In this dissertation, we first introduced the general terminologies and concepts that are often used to describe the light scattering problem. Then we simulated the underwater polarized light field using a Backward Monte Carlo method and studied the effect of both coherent and incoherent beams for particulate media in biological tissues.

In Chapter 3, we have developed a backward Monte Carlo Vector method for the atmosphere-ocean system, which can be used not only to study ocean polarization but also to simulate underwater imaging. Polarization information contains a lot of useful information about the surrounding light field. Especially, for a weak scattering case, we obtained the very sharp and clear underwater image from the DOP information while radiance image only tells the four blurred spheres. Sometimes polarization itself can convey more surrounding information than the radiance. Thus it's a good option to use the light polarization to improve the underwater imaging. Since many marine animals are sensitive to polarization, the extended study of their ability to detect and to utilize light polarization in the ocean is of great application potential. This code can also be used to simulate polarized light field scattering in other circumstances, such as to detect a tumor in healthy tissues and to make a 3D light field animation in the real world. In the future, we can include a dynamic surface in the code to study the impact of ocean waves on the underwater imaging and remote sensing.

In Chapter 4, We have studied both forward and multiple scattering for granular media in many biological organisms. The scattering in the forward direction is always coherent, regardless of the shapes, the sizes, as well as the orientations of scatterers, which will result in a big forward scattering peak for an ensemble of particles. With decreased coherence lengths of the incident wave, the phase function forward peak will decrease due to lost

coherence. For sparsely packed particles inside a large volume, for example, aerosols in the atmosphere, with decreased coherence lengths of the incident wave, the multiple scattering can be approximated by radiative transfer theory since only particles inside the coherence volume will add coherently and the non-coherent treatment is valid. However, approximating an organism by a homogeneous medium with the EMT theory is not valid since the organic particles are too large to make the scattering medium a continuum.

REFERENCES

[1] Gilbert, G. D. & Pernicka, J. C. Improvement of underwater visibility by reduction of backscatter with a circular polarization technique. *Applied Optics* **6**, 741–746 (1967).

[2] Cariou, J., Le Jeune, B., Lotrian, J. & Guern, Y. Polarization effects of seawater and underwater targets. *Applied Optics* **29**, 1689–1695 (1990).

[3] Chang, P., Walker, J., Hopcraft, K., Ablitt, B. & Jakeman, E. Polarization discrimination for active imaging in scattering media. *Optics Communications* **159**, 1–6 (1999).

[4] Walker, J. G., Chang, P. C. & Hopcraft, K. I. Visibility depth improvement in active polarization imaging in scattering media. *Applied Optics* **39**, 4933–4941 (2000).

[5] Chang, P. C. *et al.* Improving visibility depth in passive underwater imaging by use of polarization. *Applied Optics* **42**, 2794–2803 (2003).

[6] Waterman, T. H. Polarization patterns in submarine illumination. *Science* **120**, 927–932 (1954).

[7] Walraven, R. Polarization imagery. *Optical Engineering* **20**, 200114–200114 (1981).

[8] Flamarique, I. N. & Hárosi, F. I. Visual pigments and dichroism of anchovy cones: a model system for polarization detection. *Visual Neuroscience* **19**, 467–473 (2002).

[9] Shashar, N. *et al.* Underwater linear polarization: physical limitations to biological functions. *Philosophical Transactions of the Royal Society B: Biological Sciences* **366**, 649–654 (2011).

[10] Shashar, N., Hagan, R., Boal, J. G. & Hanlon, R. T. Cuttlefish use polarization sensitivity in predation on silvery fish. *Vision Research* **40**, 71–75 (2000).

[11] Mäthger, L. M. & Hanlon, R. T. Anatomical basis for camouflaged polarized light communication in squid. *Biology Letters* **2**, 494–496 (2006).

[12] Chiou, T.-H. *et al.* Circular polarization vision in a stomatopod crustacean. *Current Biology* **18**, 429–434 (2008).

[13] Chandrasekhar, S. *Radiative transfer* (Courier Corporation, 2013).

[14] Mishchenko, M. I., Travis, L. D. & Lacis, A. A. *Scattering, absorption, and emission of light by small particles* (Cambridge University Press, 2002).

[15] Twomey, S., Jacobowitz, H. & Howell, H. Matrix methods for multiple-scattering problems. *Journal of Atmospheric Sciences* **23**, 289–298 (1966).

[16] Plass, G. N., Kattawar, G. W. & Catchings, F. E. Matrix operator theory of radiative transfer. 1: Rayleigh scattering. *Applied Optics* **12**, 314–329 (1973).

[17] Kattawar, G. W., Plass, G. N. & Catchings, F. E. Matrix operator theory of radiative transfer. 2: Scattering from maritime haze. *Applied Optics* **12**, 1071–1084 (1973).

[18] Zhai, P.-W. *et al.* A vector radiative transfer model for coupled atmosphere and ocean systems with a rough interface. *Journal of Quantitative Spectroscopy and Radiative Transfer* **111**, 1025–1040 (2010).

[19] O'Brien, D. Accelerated quasi monte carlo integration of the radiative transfer equation. *Journal of Quantitative Spectroscopy and Radiative Transfer* **48**, 41–59 (1992).

[20] Sánchez, A., Smith, T. & Krajewski, W. A three-dimensional atmospheric radiative transfer model based on the discrete-ordinates method. *Atmospheric Research* **33**, 283–308 (1994).

[21] Haferman, J. L., Smith, T. F. & Krajewski, W. F. A multi-dimensional discrete-ordinates method for polarized radiative transfer. part i: validation for randomly ori-

ented axisymmetric particles. *Journal of Quantitative Spectroscopy and Radiative Transfer* **58**, 379–398 (1997).

[22] Chen, Y., Liou, K. & Gu, Y. An efficient diffusion approximation for 3d radiative transfer parameterization: application to cloudy atmospheres. *Journal of Quantitative Spectroscopy and Radiative Transfer* **92**, 189–200 (2005).

[23] Zhai, P.-W., Kattawar, G. W. & Yang, P. Impulse response solution to the three-dimensional vector radiative transfer equation in atmosphere-ocean systems. i. monte carlo method. *Applied Optics* **47**, 1037–1047 (2008).

[24] Zhai, P.-W., Kattawar, G. W. & Yang, P. Impulse response solution to the three-dimensional vector radiative transfer equation in atmosphere-ocean systems. ii. the hybrid matrix operator–monte carlo method. *Applied Optics* **47**, 1063–1071 (2008).

[25] You, Y., Zhai, P.-W., Kattawar, G. W. & Yang, P. Polarized radiance fields under a dynamic ocean surface: a three-dimensional radiative transfer solution. *Applied Optics* **48**, 3019–3029 (2009).

[26] Cloney, R. A. & Florey, E. Ultrastructure of cephalopod chromatophore organs. *Cell and Tissue Research* **89**, 250–280 (1968).

[27] Messenger, J. B. Cephalopod chromatophores: neurobiology and natural history. *Biological Reviews* **76**, 473–528 (2001).

[28] Bosschaart, N., Edelman, G. J., Aalders, M. C., van Leeuwen, T. G. & Faber, D. J. A literature review and novel theoretical approach on the optical properties of whole blood. *Lasers in Medical Science* **29**, 453–479 (2014).

[29] Mishchenko, M. I., Travis, L. D. & Lacis, A. A. *Multiple scattering of light by particles: radiative transfer and coherent backscattering* (Cambridge University Press, 2006).

[30] Deravi, L. F. *et al.* The structure–function relationships of a natural nanoscale photonic device in cuttlefish chromatophores. *Journal of The Royal Society Interface* **11**, 20130942 (2014).

[31] Sydoruk, O., Zhernovaya, O., Tuchin, V. & Douplik, A. Refractive index of solutions of human hemoglobin from the near-infrared to the ultraviolet range: Kramers-kronig analysis. *Journal of Biomedical Optics* **17**, 115002–115002 (2012).

[32] Mie, G. Articles on the optical characteristics of turbid tubes, especially colloidal metal solutions. *Ann. Phys* **25**, 377–445 (1908).

[33] Draine, B. T. The discrete-dipole approximation and its application to interstellar graphite grains. *The Astrophysical Journal* **333**, 848–872 (1988).

[34] Yurkin, M. A. & Hoekstra, A. G. The discrete dipole approximation: an overview and recent developments. *Journal of Quantitative Spectroscopy and Radiative Transfer* **106**, 558–589 (2007).

[35] Yee, K. S. *et al.* Numerical solution of initial boundary value problems involving maxwell's equations in isotropic media. *IEEE Trans. Antennas Propag* **14**, 302–307 (1966).

[36] Yang, P. & Liou, K. Finite-difference time domain method for light scattering by small ice crystals in three-dimensional space. *JOSA A* **13**, 2072–2085 (1996).

[37] Johnson, B. R. Invariant imbedding t matrix approach to electromagnetic scattering. *Applied Optics* **27**, 4861–4873 (1988).

[38] Bi, L., Yang, P., Kattawar, G. W. & Mishchenko, M. I. Efficient implementation of the invariant imbedding t-matrix method and the separation of variables method applied to large nonspherical inhomogeneous particles. *Journal of Quantitative Spectroscopy and Radiative Transfer* **116**, 169–183 (2013).

[39] Ishimaru, A. *Wave propagation and scattering in random media*, vol. 2 (Academic Press New York, 1978).

[40] Mackowski, D. & Mishchenko, M. A multiple sphere t-matrix fortran code for use on parallel computer clusters. *Journal of Quantitative Spectroscopy and Radiative Transfer* **112**, 2182–2192 (2011).

[41] Wolf, E. *Introduction to the theory of coherence and polarization of light* (Cambridge University Press, 2007).

[42] Shirai, T., Dogariu, A. & Wolf, E. Mode analysis of spreading of partially coherent beams propagating through atmospheric turbulence. *JOSA A* **20**, 1094–1102 (2003).

[43] Gbur, G. & Wolf, E. Spreading of partially coherent beams in random media. *JOSA A* **19**, 1592–1598 (2002).

[44] Bohren, C. F. & Huffman, D. R. *Absorption and scattering of light by small particles* (John Wiley & Sons, 2008).

[45] Hulst, H. C. & van de Hulst, H. C. *Light scattering by small particles* (Courier Corporation, 1957).

[46] Anderson, D. G. & Barakat, R. Necessary and sufficient conditions for a mueller matrix to be derivable from a jones matrix. *JOSA A* **11**, 2305–2319 (1994).

[47] Fry, E. S. & Kattawar, G. W. Relationships between elements of the stokes matrix. *Applied Optics* **20**, 2811–2814 (1981).

[48] Henyey, L. G. & Greenstein, J. L. Diffuse radiation in the galaxy. *The Astrophysical Journal* **93**, 70–83 (1941).

[49] Mobley, C. D. *Light and water: radiative transfer in natural waters* (Academic Press, 1994).

[50] Zege, E. P., Polonsky, I. N. *et al.* Multicomponent approach to light propagation in clouds and mists. *Applied Optics* **32**, 2803–2812 (1993).

[51] Liu, J., Bi, L., Yang, P. & Kattawar, G. W. Scattering of partially coherent electromagnetic beams by water droplets and ice crystals. *Journal of Quantitative Spectroscopy and Radiative Transfer* **134**, 74–84 (2014).